

Supplementary Material for “Observation of unconventional many-body scarring in a quantum simulator”

Guo-Xian Su,^{1,2,3} Hui Sun,^{1,2,3} Ana Hudomal,⁴ Jean-Yves Desaulles,⁴ Zhao-Yu Zhou,^{1,2,3}
 Bing Yang,⁵ Jad C. Halimeh,⁶ Zhen-Sheng Yuan,^{1,2,3} Zlatko Papić,⁴ and Jian-Wei Pan^{1,2,3}

¹*Hefei National Laboratory for Physical Sciences at Microscale and Department of Modern Physics,
 University of Science and Technology of China, Hefei, Anhui 230026, China*

²*Physikalisches Institut, Ruprecht-Karls-Universität Heidelberg,
 Im Neuenheimer Feld 226, 69120 Heidelberg, Germany*

³*CAS Center for Excellence and Synergetic Innovation Center in Quantum Information and Quantum Physics,
 University of Science and Technology of China, Hefei, Anhui 230026, China*

⁴*School of Physics and Astronomy, University of Leeds, Leeds LS2 9JT, UK*

⁵*Department of Physics, Southern University of Science and Technology, Shenzhen 518055, China*

⁶*INO-CNR BEC Center and Department of Physics,
 University of Trento, Via Sommarive 14, I-38123 Trento, Italy*

CONTENTS

I. MAPPING THE TILTED 1D BOSE-HUBBARD ONTO THE PXP MODEL

I. Mapping the tilted 1D Bose-Hubbard onto the PXP model

- A. $\Delta \approx U$ resonance: first order terms
- B. Higher order terms in the mapping

II. Numerical methods

- A. Numerical demonstrations of the mapping between PXP and tilted Bose-Hubbard model

III. Global vs. single-site fidelity

IV. Alternative mapping between PXP and tilted 1D Bose-Hubbard with staggered detuning

V. Effect of periodic driving on \mathbb{Z}_2 scars

- A. Driven PXP model
- B. Driving the tilted 1D Bose-Hubbard model

VI. Quantum many-body scars in the polarized state

- A. Pure PXP model
- B. Static detuning in the PXP model
- C. Periodic driving in the PXP model
- D. Detuning and periodic driving in the tilted Bose-Hubbard model

VII. Other quantum many-body scarred states

VIII. Effect of detuning on the spectral statistics of the PXP model

IX. System-size scaling of the revival fidelity

References

In the main text and throughout this Supplementary Material, we study the 1D Bose-Hubbard model with linear tilt potential and open boundary conditions, described by the Hamiltonian

$$\hat{H} = -J \sum_{i=1}^{L-1} \left(\hat{b}_i^\dagger \hat{b}_{i+1} + \hat{b}_{i+1}^\dagger \hat{b}_i \right) + \frac{U}{2} \underbrace{\sum_{i=1}^L \hat{n}_i (\hat{n}_i - 1)}_{\hat{H}_U} + \Delta \underbrace{\sum_{i=1}^L i \hat{n}_i}_{\hat{H}_\Delta} \quad (1)$$

where J is the hopping amplitude, U is the interaction strength, Δ is the tilt and L the number of sites. Unless specified otherwise, we fix the filling factor to $\nu = 1$, i.e., the number of bosons is equal to the number of sites in the chain.

A. $\Delta \approx U$ resonance: first order terms

In the $U, \Delta \gg J$ limit, the energy spectrum of the Hamiltonian in Eq. (1) splits into bands with approximately constant expectation value of the diagonal terms, $\langle \hat{H}_U + \hat{H}_\Delta \rangle \approx \text{const}$, and the Hilbert space becomes fragmented. At the $U \approx \Delta \gg J$ resonance, the only process which conserves $\langle \hat{H}_U + \hat{H}_\Delta \rangle$ is $11 \leftrightarrow 20$, i.e. doublons can only be created by moving a particle to the left and destroyed by moving a particle to the right. In the connected component of the Fock state $111 \dots 111$, the system in the resonant regime can therefore be described by an effective Hamiltonian

$$\hat{H}_{\text{eff}} = -J \sum_{i=1}^{L-1} \left(\hat{b}_i^\dagger \hat{b}_{i+1} \hat{n}_i (2 - \hat{n}_i) \hat{n}_{i+1} (2 - \hat{n}_{i+1}) + \text{h.c.} \right). \quad (2)$$

The Hamiltonian (2) is equivalent to the PXP Hamiltonian [1, 2], as will be shown below (see also Ref. [3])

1 for the original derivation of the mapping and a recent 37
2 review [4]). 38

3 The connected component of the Hilbert space con- 39
4 tains only certain types of two-site configurations (20, 40
5 11, 12, 02, 01), while all other two-site configurations are 41
6 forbidden (22, 21, 10, 00). If we consider the configura- 42
7 tion 20 to be an excitation, all allowed configurations can 43
8 be mapped to those of the PXP model as follows: 44

$$\begin{aligned}
 \dots 20 \dots &\leftrightarrow \bullet \circ \bullet \circ \\
 \dots 11 \dots &\leftrightarrow \circ \circ \circ \circ \\
 \dots 12 \dots &\leftrightarrow \circ \circ \bullet \\
 \dots 02 \dots &\leftrightarrow \bullet \circ \bullet \\
 \dots 01 \dots &\leftrightarrow \bullet \circ \circ
 \end{aligned} \tag{3}$$

9 Note that excitations live on the bonds between sites and 51
10 this mapping also includes links to the two surrounding 52
11 sites. For example, the configuration $\dots 2020 \dots$ maps to 53
12 $\circ \bullet \circ \bullet \circ$ and not to $\circ \bullet \circ \circ \bullet \circ$. On the other hand, the 54
13 configuration 2020 with open boundaries on both sides 55
14 maps to $\bullet \circ \bullet$, as there are no bonds across the boundaries. 56

15 The effective Hamiltonian (2) can be rewritten as: 57

$$\hat{H}_{\text{eff}} = -J \sum_{i=1}^{L-1} \left(\underbrace{\hat{b}_i^\dagger \hat{b}_{i+1} \delta_{\hat{n}_i, 1} \delta_{\hat{n}_{i+1}, 1}}_{\sqrt{2} \hat{P}_{j-1} \hat{\sigma}_j^+ \hat{P}_{j+1}} + \underbrace{\hat{b}_{i+1}^\dagger \hat{b}_i \delta_{\hat{n}_i, 2} \delta_{\hat{n}_{i+1}, 0}}_{\sqrt{2} \hat{P}_{j-1} \hat{\sigma}_j^- \hat{P}_{j+1}} \right). \tag{4}$$

16 In this equation, the index i labels the sites, while j labels 58
17 the bonds between sites. The Kronecker delta functions 59
18 have been expressed in terms of projectors, $\hat{P}_j = |\circ_j\rangle\langle\circ_j|$, 60
19 and the bosonic hopping terms correspond to the spin 61
20 raising and lowering operators, $\hat{\sigma}_j^\pm$, on the bond j . We
21 can use delta functions because there are no configura- 62
22 tions with more than 2 particles per site in this connected 63
23 component and the only possible values of $\hat{n}_i(2 - \hat{n}_i)$ are
24 0 and 1. Moving a particle to a neighboring site on the
25 left corresponds to creating an excitation, moving to the
26 right to annihilating, while the delta functions act as con-
27 straints.

28 Finally, the effective Hamiltonian is therefore equiva- 64
29 lent to the PXP Hamiltonian 65

$$\begin{aligned}
 \hat{H}_{\text{PXP}} &= \Omega \sum_{j=1}^N \left(\hat{P}_{j-1} \hat{\sigma}_j^+ \hat{P}_{j+1} + \hat{P}_{j-1} \hat{\sigma}_j^- \hat{P}_{j+1} \right) \\
 &= \Omega \sum_{j=1}^N \hat{P}_{j-1} \hat{X}_j \hat{P}_{j+1},
 \end{aligned} \tag{5}$$

30 when $\Omega = \sqrt{2}J$ and $N = L - 1$, where $\hat{X}_j \equiv |\circ_j\rangle\langle\bullet_j| +$
31 $|\bullet_j\rangle\langle\circ_j|$ is the usual Pauli x matrix. In case of open
32 boundary conditions (OBC) the two boundary terms be-
33 come $\hat{X}_1 \hat{P}_2$ and $\hat{P}_{N-1} \hat{X}_N$. Note that the effective bosonic 69
34 model for system size L is equivalent to the PXP model 70
35 for size $N = L - 1$ since the number of bonds is the 71
36 number of sites minus one. 72

In the PXP model, the initial states which lead to
pronounced quantum revivals are the two states with
the maximal number of excitations – the Néel states,
 $\bullet \circ \bullet \circ \dots \bullet \circ$ and $\circ \bullet \circ \bullet \dots \circ \bullet$ [5, 6]. The equivalent states
in the tilted Bose-Hubbard model are 2020...201 and
12020...20 for odd system sizes and 2020...20 and
120...201 for even sizes. In our experimental setup, it is
not possible to exactly prepare the 2020...201 state due
to the inability to independently control single sites. In-
stead, our experiment realizes the 2020...20 state, which
corresponds to the Néel state $\bullet \circ \bullet \circ \dots \bullet \circ \bullet$ in the PXP
model with an odd number of sites and open boundary
conditions.

B. Higher order terms in the mapping

The effective Hamiltonian of Eq. (2) results from the
first-order Schrieffer-Wolff transformation [7] where $\hat{H}_0 =$
 $\hat{H}_U + \hat{H}_\Delta$. In this section we look at the relevant terms
that arise in the effective Hamiltonian at second order.
To simplify the notation we write these terms as sums of
range-3 operators, where $|111\rangle\langle 120|_j$ denotes the opera-
tor changing sites $j-1, j$ and $j+1$ from 120 to 111 while
leaving all other sites unaffected.

First, we can identify the matrix elements that take
the system out of the PXP sector. This happens by the
appearance of sites with 3 bosons via the operator

$$\begin{aligned}
 \hat{H}_{\text{out}} &= \frac{\sqrt{3}J^2}{U} \sum_{j=2}^{L-1} \left(|300\rangle\langle 201|_j + |201\rangle\langle 300|_j \right. \\
 &\quad \left. + 2|300\rangle\langle 120|_j + 2|120\rangle\langle 300|_j \right).
 \end{aligned} \tag{6}$$

There are also off-diagonal matrix elements connecting
states within the PXP sector, given by

$$\hat{H}_{\text{OD}} = \frac{2J^2}{U} \sum_{j=2}^{L-1} \left(|120\rangle\langle 201|_j + |201\rangle\langle 120|_j \right). \tag{7}$$

There are also additional off-diagonal matrix elements
connecting states outside of the PXP sector, but as they
do not directly influence the dynamics out of it we do not
describe them here.

Finally, the diagonal operator in this sector is given by

$$\begin{aligned}
 \hat{H}_{\text{Diag}} &= \frac{J^2}{U} \sum_{j=2}^{L-1} \left(4|120\rangle\langle 120|_j - |111\rangle\langle 111|_j \right. \\
 &\quad \left. + |020\rangle\langle 020|_j - |112\rangle\langle 112|_j \right) \\
 &\quad + \frac{J^2}{U} \left(|01\rangle\langle 01|_{L-1} - |11\rangle\langle 11|_1 - |12\rangle\langle 12|_1 \right),
 \end{aligned} \tag{8}$$

where the two-site operator $|11\rangle\langle 12|_j$ acts on sites j and
 $j+1$. As bulk terms get added, the overall diagonal
factors are extensive in the system size in the Fock basis.
The state with the lowest on-site potential is $|111\dots 11\rangle$

with a value of $-\frac{(L-1)J^2}{U}$. The maximum is $\approx \frac{4J^2L}{3U}$ for the state $|120120\dots 120\rangle$, which corresponds to the \mathbb{Z}_3 state in the PXP terminology.

In order to see how these second-order terms change the effective model we can rewrite Eqs. (7)-(8) for the PXP model with $N = L - 1$ sites. To do this we introduce the single-site projector on the excited state $\hat{Q}_j = |\bullet\rangle\langle\bullet| = \mathbf{1} - \hat{P}_j$. We then obtain

$$\begin{aligned} \hat{H}_{\text{OD}}^{\text{PXP}} = & \frac{2J^2}{U} \sum_{j=1}^{N-2} \left(\hat{P}_{j-1} \hat{\sigma}_j^+ \hat{\sigma}_{j+1}^- \hat{P}_{j+2} + \hat{P}_{j-1} \hat{\sigma}_j^- \hat{\sigma}_{j+1}^+ \hat{P}_{j+2} \right) \\ & + \frac{2J^2}{U} \left(\hat{\sigma}_1^+ \hat{\sigma}_2^- \hat{P}_3 + \hat{\sigma}_1^- \hat{\sigma}_2^+ \hat{P}_3 \right) \\ & + \frac{2J^2}{U} \left(\hat{P}_{N-3} \hat{\sigma}_{N-1}^+ \hat{\sigma}_N^- + \hat{P}_{N-2} \hat{\sigma}_{N-1}^- \hat{\sigma}_N^+ \right) \end{aligned} \quad (9)$$

and

$$\begin{aligned} \hat{H}_{\text{Diag}}^{\text{PXP}} = & \frac{J^2}{U} \sum_{j=1}^{N-2} \left(4\hat{P}_{j-1} \hat{P}_j \hat{Q}_{j+1} \hat{P}_{j+2} - \hat{P}_{j-1} \hat{P}_j \hat{P}_{j+1} \hat{P}_{j+2} \right. \\ & + \hat{Q}_{j-1} \hat{P}_j \hat{Q}_{j+1} \hat{P}_{j+2} - \hat{P}_{j-1} \hat{P}_j \hat{P}_{j+1} \hat{Q}_{j+2} \left. \right) \\ & + \frac{J^2}{U} \left(4\hat{P}_0 \hat{Q}_1 \hat{P}_2 - \hat{P}_0 \hat{P}_1 \hat{P}_2 - \hat{P}_0 \hat{P}_1 \hat{Q}_2 \right. \\ & + 4\hat{P}_{N-2} \hat{P}_{N-1} \hat{Q}_N - \hat{P}_{N-2} \hat{P}_{N-1} \hat{P}_N \\ & + \hat{Q}_{N-2} \hat{P}_{N-1} \hat{Q}_N \left. \right) \\ & + \frac{J^2}{U} \left(\hat{Q}_{N-1} \hat{P}_N - \hat{P}_0 \hat{P}_1 - \hat{P}_0 \hat{Q}_1 \right), \end{aligned} \quad (10)$$

respectively. We notice that the off-diagonal correction has the form of a constrained XY term.

II. NUMERICAL METHODS

In the main text and this Supplementary Material, we use two types of numerical methods for modeling the experiment. For small Bose-Hubbard chains with $L \lesssim 12$ sites, we use exact diagonalization techniques to obtain the full energy spectrum of the Hamiltonian and directly access the system's eigenstate properties. Unless specified otherwise, we restrict the occupancy of any site to be at maximum 3 bosons, as our results are found to be insensitive to allowing more than 3 bosons on any site.

To access dynamics in much larger systems, $L \lesssim 50$ sites, we use TEBD variational method [8] implemented in TenPy package [9]. We employ the second order Trotter decomposition with time step $2.5 \times 10^{-5}/J$ and maximum bond dimension $\chi_{\text{max}} = 3000$. Such a small time step was necessary because some of the quantities we are interested in, e.g., the fidelity density, are sensitive to otherwise negligible fluctuations in the revival peak heights that appear for longer time steps.

For numerical simulations via either one of these methods, it is convenient to work in natural units $\hbar=1$. We

adopt this convention for presenting all numerical results in this Supplementary Material.

A. Numerical demonstrations of the mapping between PXP and tilted Bose-Hubbard model

In this Section, we numerically corroborate the mapping between PXP and Bose-Hubbard models introduced in Sec. I. Specifically, we use exact diagonalization to demonstrate the consistency between dynamics and eigenstate properties in the PXP model and the Bose-Hubbard model tuned to the resonance $U=\Delta$.

In analogy with the PXP model, the system initialized in the state $2020\dots 201$ is expected to oscillate between this state and the state $12020\dots 20$. This is not only the case for the effective model (4) which is exactly equivalent to PXP, but also for the full tilted Bose-Hubbard model (1) at the $U = \Delta$ resonance, as can be observed in Fig. 1.

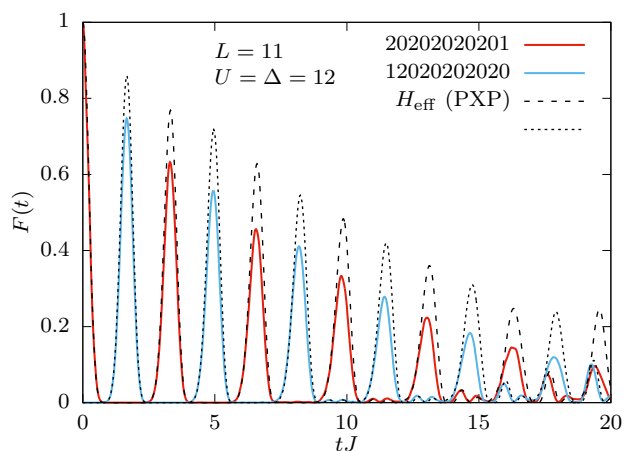


FIG. 1. Evolution of quantum fidelity $F(t) = |\langle\psi_0|e^{-iHt}|\psi_0\rangle|^2$ starting from the state $|\psi_0\rangle = |2020\dots 201\rangle$ (red) and the amplitude of state transfer, $\mathcal{O}(t) = |\langle\psi|e^{-iHt}|\psi_0\rangle|^2$, with the state $|\psi\rangle = |12020\dots 20\rangle$ (blue). The evolution is governed by the tilted Bose-Hubbard Hamiltonian in Eq. (1) with $J=1$, $U=\Delta=12$ and maximally 3 particles per site. The dashed and dotted black lines correspond to the effective model in Eq. (4). System size $L=11$, filling factor $\nu=1$.

In Fig. 2 we show the evolution of the bipartite von Neumann entanglement entropy, $S_{\text{vN}}(t) = -\text{Tr}_A(\hat{\rho}_A \ln \hat{\rho}_A)$, where $\hat{\rho}_A$ is the reduced density matrix for subsystem A of length L_A . The system is initially prepared in the state $2020\dots 201$ or the completely homogeneous state $111\dots 111$. As in the PXP model, the entanglement entropy for the $2020\dots 201$ state exhibits slow and approximately linear growth in time. In contrast, the entanglement entropy for the state $111\dots 111$ rapidly saturates, implying that the system quickly thermalizes.

The evolution of density imbalance between the even and odd sites $\langle\hat{M}_z\rangle = (\langle\hat{n}_{\text{odd}}\rangle - \langle\hat{n}_{\text{even}}\rangle)/(\langle\hat{n}_{\text{odd}}\rangle + \langle\hat{n}_{\text{even}}\rangle)$, which corresponds to staggered magnetization

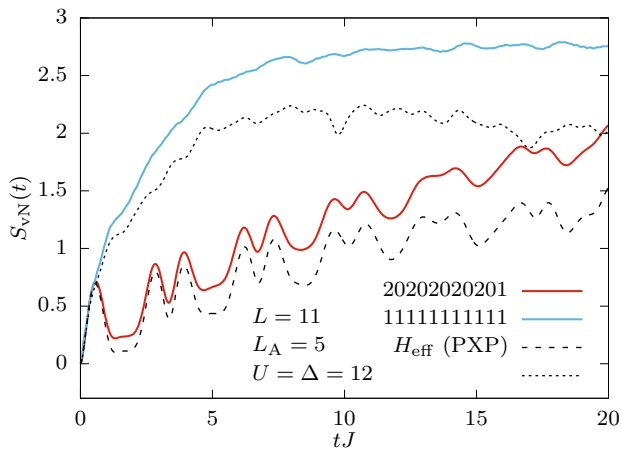


FIG. 2. Evolution of the bipartite entanglement entropy for the initial states $|2020\dots 201\rangle$ (red) and $|111\dots 111\rangle$ (blue). The evolution is governed by the tilted Bose-Hubbard Hamiltonian from Eq. (1) with $J = 1$, $U = \Delta = 12$ and maximally 3 particles per site. The dashed and dotted black lines correspond to the effective model from Eq. (4). System size $L = 11$, subsystem $L_A = 5$, filling factor $\nu = 1$.

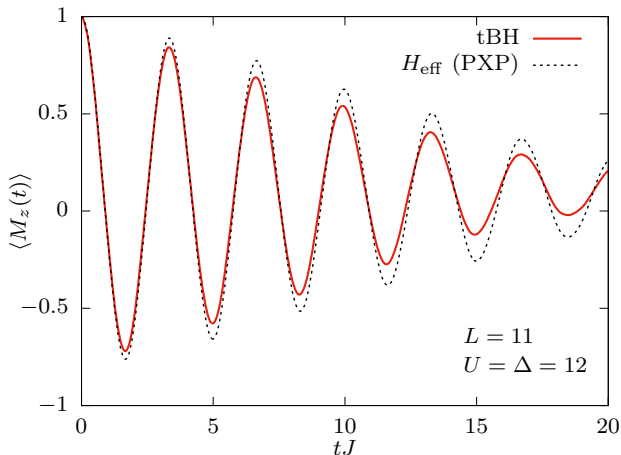


FIG. 3. Evolution of staggered magnetization $\langle \hat{M}_z \rangle = (\langle \hat{n}_{\text{odd}} \rangle - \langle \hat{n}_{\text{even}} \rangle) / (\langle \hat{n}_{\text{odd}} \rangle + \langle \hat{n}_{\text{even}} \rangle)$, where \hat{n}_{odd} and \hat{n}_{even} are the numbers of particles on odd and even sites. The evolution is governed by the tilted Bose-Hubbard Hamiltonian from Eq. (1) with $J = 1$ and $U = \Delta = 12$ (solid red line) and the effective model from Eq. (4) which is equivalent to the PXP model (dashed black line). System size $L = 11$, filling factor $\nu = 1$, initial state $|2020\dots 201\rangle$.

1 in the PXP model, is shown in Fig. 3. This is one of the
 2 quantities that was experimentally measured in the main
 3 text. Here we again compare the evolution with the full
 4 tilted Bose-Hubbard Hamiltonian (1) and the effective
 5 Hamiltonian (4), the latter being equivalent to the PXP
 6 model, and we find excellent agreement between the two.
 7 The overlap of eigenstates in the full model in Eq. (1)
 8 for a chain of $L = 9$ sites with the initial $|202020201\rangle$
 9 state is given in Fig. 4. For parameter values $U = \Delta = 12$,
 10 and $J = 1$, the energy spectrum is split into multi-

11 ple bands with approximately constant expectation value
 12 of the sum of interaction and tilt terms $\langle \hat{H}_U + \hat{H}_\Delta \rangle$,
 13 as indicated by different colors. The inset shows the
 14 top part of the highest-overlap band (around $E =$
 15 $\langle 202020201 | \hat{H} | 202020201 \rangle = 432$). This band is de-
 16 scribed by the effective Hamiltonian (2), which preserves
 17 the expectation value $\langle \hat{H}_U + \hat{H}_\Delta \rangle$ and is equivalent to the
 18 PXP Hamiltonian. A band of $L = 9$ scarred eigenstates
 19 is visible in the inset, as expected from the analogy with
 20 the PXP model. These scarred eigenstates are responsi-
 21 ble for the revival dynamics in Fig. 1. As the two Néel
 22 states have the maximal number of doublons at filling
 23 factor $\nu = 1$, this type of dynamics also leads to oscil-
 24 lations in doublon number, which can be experimentally
 25 measured.

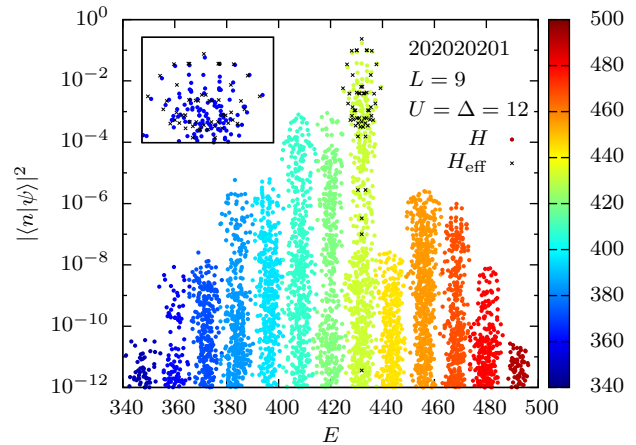


FIG. 4. Overlap of the state $|202020201\rangle$ with the eigenstates of the tilted Bose-Hubbard model (1) with $J = 1$ and $U = \Delta = 12$. The colors indicate the expectation value of the diagonal terms $\langle \hat{H}_U + \hat{H}_\Delta \rangle$ for each eigenstate. The black crosses correspond to the effective model (4) (shifted by $E = \langle 202020201 | \hat{H} | 202020201 \rangle = 432$). The inset shows the top part of band with the highest overlap, where a band of $L = 9$ scarred eigenstates analogous to that in the PXP model can be seen.

As a side note, the system is also described by PXP-
 like effective models at other integer filling factors. The
 reviving initial states are of the form $|(n+1)(n-1)(n+1)(n-1)\dots(n+1)(n-1)n\rangle$ for $\nu = n$, e.g. $|3131\dots 312\rangle$
 for $\nu = 2$ and $|4242\dots 423\rangle$ for $\nu = 3$, as shown in Fig. 5.
 Revival frequency increases with n as $\sqrt{n(n-1)}$, but the
 revivals decay faster for larger n .

III. GLOBAL VS. SINGLE-SITE FIDELITY

In this section we discuss the relation between two
 measures of similarity of pure states used in this work.
 One measure is the quantum fidelity

$$\mathcal{F}(|\phi\rangle, |\psi\rangle) = |\langle \phi | \psi \rangle|^2, \quad (11)$$

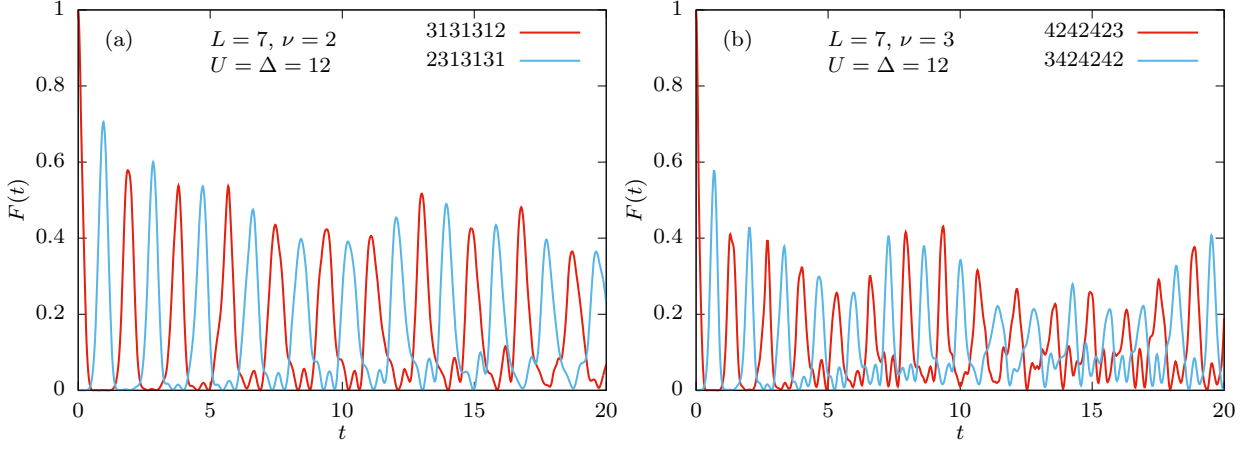


FIG. 5. Evolution of quantum fidelity $F(t) = |\langle \psi_0 | e^{-iHt} | \psi_0 \rangle|^2$ starting from the Néel state $|\psi_0\rangle$ (red) and the amplitude of state transfer, $\mathcal{O}(t) = |\langle \psi | e^{-iHt} | \psi_0 \rangle|^2$, for the anti-Néel state $|\psi\rangle$ (blue). The evolution is governed by the tilted Bose-Hubbard Hamiltonian from Eq. (1) with $J = 1$ and $U = \Delta = 12$. (a) Filling factor $\nu = 2$. (b) $\nu = 3$. The Hilbert space size is reduced by removing the configurations with more than 3 particles per site in (a) and more than 4 particles per site in (b).

i.e., the global overlap between two pure states. This measure is very convenient for numerical simulations and theoretical analysis, but hard to measure in experiment. For this reason, we also consider a different measure consisting of an average of local measurements:

$$\mathcal{F}_{(r)}(|\phi\rangle, |\psi\rangle) = \frac{1}{L+1-r} \sum_{j=1}^{L+1-r} \text{Tr} \left[\hat{\rho}_{j,j+r-1}^{\phi} \hat{\rho}_{j,j+r-1}^{\psi} \right], \quad (12)$$

where $1 \leq r \leq L$ is the range of the measurements and

$$\hat{\rho}_{j,j+r-1}^{\phi} = \text{Tr}_{\perp, j, j+r-1} [|\phi\rangle \langle \phi|] \quad (13)$$

is the density matrix obtained by performing the partial trace on all sites except sites j to $j-1+r$.

Both quantities, \mathcal{F} and $\mathcal{F}_{(r)}$, are real and obey

$$0 \leq \mathcal{F}(|\phi\rangle, |\psi\rangle), \mathcal{F}_{(r)}(|\phi\rangle, |\psi\rangle) \leq 1, \quad (14)$$

and

$$\mathcal{F}_{(r)}(|\phi\rangle, |\psi\rangle) = \mathcal{F}_{(r)}(|\psi\rangle, |\phi\rangle), \quad (15)$$

$$\mathcal{F}(|\phi\rangle, |\psi\rangle) = \mathcal{F}(|\psi\rangle, |\phi\rangle). \quad (16)$$

It is also important to note that

$$\begin{aligned} \mathcal{F}_{(L)}(|\phi\rangle, |\psi\rangle) &= \text{Tr} [|\phi\rangle \langle \phi| \psi\rangle \langle \psi|] \\ &= |\langle \phi | \psi \rangle|^2 = \mathcal{F}(|\phi\rangle, |\psi\rangle). \end{aligned} \quad (17)$$

While for arbitrary states $\mathcal{F}_{(r)}$ is neither an upper bound nor a lower bound of \mathcal{F} , it does not mean that this is never the case. We are now limiting our study to the case where the state ϕ is a product state. The consequence of that is that the reduced density matrix $\hat{\rho}_{j,j+r-1}^{\phi}$ will correspond to a pure state for any r . We can then choose a basis for each site such that $|\phi\rangle$ is a product of local basis states, and so a Fock basis state for the whole Hilbert space. Let us then denote the orthonormal states of this basis by $|\alpha\rangle$.

This allows us to rewrite the reduced density matrix as $\hat{\rho}_{j,j+r-1}^{\phi} = |\phi_{j,j+r-1}\rangle \langle \phi_{j,j+r-1}|$, where $|\phi_{j,j+r-1}\rangle$ corresponds to the state ϕ for sites j to $j+r-1$ (remember that we can only do this because $|\phi\rangle$ is a product state). This formulation implies the following simplification

$$\begin{aligned} \mathcal{F}_{(r)}(|\phi\rangle, |\psi\rangle) &= \frac{1}{L+1-r} \sum_{j=1}^{L+1-r} \text{Tr} \left[\hat{\rho}_{j,j+r-1}^{\phi} \hat{\rho}_{j,j+r-1}^{\psi} \right] \\ &= \frac{1}{L+1-r} \sum_{j=1}^{L+1-r} \text{Tr} \left[|\phi_{j,j+r-1}\rangle \langle \phi_{j,j+r-1}| \hat{\rho}_{j,j+r-1}^{\psi} \right] \\ &= \frac{1}{L+1-r} \sum_{j=1}^{L+1-r} \sum_{\substack{|\alpha\rangle \text{ s.t.} \\ \langle \alpha | \phi \rangle_{j,j+r-1} = 1}} |\langle \alpha | \psi \rangle|^2 \\ &= \frac{1}{L+1-r} \sum_{|\alpha\rangle} |\langle \alpha | \psi \rangle|^2 \sum_{j=1}^{L+1-r} \prod_{k=j}^{j+r-1} \langle \alpha_k | \phi_k \rangle \\ &= |\langle \phi | \psi \rangle|^2 + \frac{1}{L+1-r} \sum_{|\alpha\rangle \neq |\phi\rangle} |\langle \alpha | \psi \rangle|^2 \sum_{j=1}^{L+1-r} \prod_{k=j}^{j+r-1} \langle \alpha_k | \phi_k \rangle \\ &\geq |\langle \phi | \psi \rangle|^2 = \mathcal{F}(|\phi\rangle, |\psi\rangle), \end{aligned} \quad (18)$$

where $\langle \alpha | \phi \rangle_{j,j+r-1}$ denotes the product of $\langle \alpha_{j,j+1-r} \rangle$ and $\langle \phi_{j,j+1-r} \rangle$, which is always either 0 or 1. This means that $|\langle \alpha | \psi \rangle|^2$ contributes to $\mathcal{F}_{(r)}(|\phi\rangle, |\psi\rangle)$ with a weight of $\frac{1}{N+1-r}$ each time r consecutive sites are in the same state in $|\alpha\rangle$ and $|\phi\rangle$. This simple rule allows us to not only derive this inequality between \mathcal{F} and $\mathcal{F}_{(r)}$, but also to compare the effect of r on $\mathcal{F}_{(r)}$. Indeed, if with r a basis state $|\alpha\rangle$ has a weight of $\frac{n}{L+1-r}$, then if $n > 0$ with $r-1$ it has a minimum weight of $\frac{n+1}{L+2-r}$. As $n \leq L+1-r$, it implies that $\frac{n}{L+1-r} \leq \frac{n+1}{L+2-r}$. If $n = 0$ then for $r-1$ the same state cannot contribute less, and so for any n it contributes more or the same amount. Hence we can

1 conclude that

$$\mathcal{F}_{(1)}(|\phi\rangle, |\psi\rangle) \geq \mathcal{F}_{(2)}(|\phi\rangle, |\psi\rangle) \geq \dots \mathcal{F}_{(L)}(|\phi\rangle, |\psi\rangle) = \mathcal{F}(|\phi\rangle, |\psi\rangle). \quad (19)$$

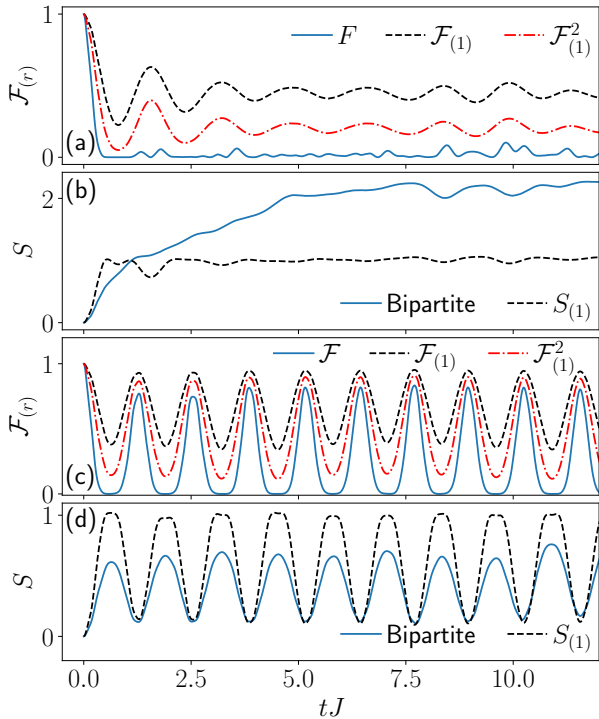


FIG. 6. Comparison between global and local quantities for the polarized state (a)-(b) without and (c)-(d) with driving. Both the single-site fidelity and the single-site entropy effectively capture the behavior of their global counterpart. In both the undriven and driven cases, the squared single-site fidelity $\mathcal{F}_{(1)}^2$ provides a better approximation of \mathcal{F} than $\mathcal{F}_{(1)}$ while still acting as an upper bound. Tilted Bose-Hubbard model (1), $J = 1$, $\Delta = U = 16$, $L = 11$, $L_A = 5$, driving parameters $U_0 = -2.38$, $U_m = 1.54$, $\omega = 4.90$.

2 Finally, it is important to note that the inequality $\frac{n}{L+1-r} \leq \frac{n+1}{L+2-r}$ is saturated if and only if $n = L + 1 - r$, meaning that $|\alpha\rangle$ and $|\phi\rangle$ are the same. This is important as $\mathcal{F}_{(r)}(|\phi\rangle, |\psi\rangle)$ is a weighted sum of all the $|\langle\alpha|\psi\rangle|^2$ with weights equal or smaller to 1. In order for $\mathcal{F}_{(r)}(|\phi\rangle, |\psi\rangle)$ to be equal to $\mathcal{F}_{(r-1)}(|\phi\rangle, |\psi\rangle)$, all weights corresponding to a non-zero $|\langle\alpha|\psi\rangle|^2$ must stay the same. But the only weights that are not increasing are either the ones that stay equal to zero or the one of $|\alpha\rangle = |\phi\rangle$ which stays equal to one. This implies that all inequalities of Eq. 19 are simultaneously saturated if and only if $|\psi\rangle = |\phi\rangle$ (in which case they are all equal to one) or $\mathcal{F}_{(1)}(|\phi\rangle, |\psi\rangle) = 0$ (in that case they are all equal to 0). It is also possible for some of them to be saturated. This can only happen if any consecutive subset of length m of $|\phi\rangle$ and $|\psi\rangle$ are orthogonal, meaning the all $\mathcal{F}_{(r)}$ are equal to 0 for all $r \geq m$.

3 In the experimental setup we only have access to the single-site fidelity $\mathcal{F}_{(1)}$, which already mimics the behav-

ior of the real fidelity \mathcal{F} (see Fig. 6). While it bounds \mathcal{F} from above, that bound is fairly loose. If we instead look at its square $\mathcal{F}_{(1)}^2$, we can see that it approximates \mathcal{F} much better as it takes a lower value when \mathcal{F} is close to zero. While $\mathcal{F}_{(1)}^2$ is not guaranteed to be an upper bound of \mathcal{F} , our theoretical simulations indicate that it still effectively acts as one for the conditions we study. Our simulations also show that the single-site second Renyi entropy $S_{(1)}$ shows a very similar behavior to the bipartite half-chain second Renyi entropy S . While it is limited in the range of values it can take, $S_{(1)}$ is clearly able to distinguish between the two regimes we are seeing in our setup: rapid entropy growth until a plateau is reached, and very slow entropy growth with oscillations on top.

IV. ALTERNATIVE MAPPING BETWEEN PXP AND TILTED 1D BOSE-HUBBARD WITH STAGGERED DETUNING

There is another mapping between the tilted 1D Bose-Hubbard and the PXP model which is based on the additional staggered potential term added to the the model in Eq. (1):

$$\hat{H} = -J \sum_{i=1}^{L-1} (\hat{b}_i^\dagger \hat{b}_{i+1} + \hat{b}_{i+1}^\dagger \hat{b}_i) + \frac{U}{2} \sum_{i=1}^L \hat{n}_i (\hat{n}_i - 1) + \Delta \sum_{i=1}^L i \hat{n}_i + \frac{\delta}{2} \sum_{i=1}^L (-1)^{i-1} \hat{n}_i. \quad (20)$$

The parameter δ determines the energy offset between even and odd lattice sites. The odd ones are now “plus” sites where the δ term is positive, while the even one are “minus” sites where it is negative. This means that for an odd chain of length L there are $N = \frac{L-1}{2}$ minus sites and $N + 1 = \frac{L+1}{2}$ plus sites.

The model in Eq. (20) has been experimentally studied (see [10] and references therein). Its mapping to the U(1) quantum link model has been already established in the literature, as is the mapping between the U(1) quantum link model and the PXP model [11]. However, the equivalence of the tilted Bose-Hubbard model with staggered detuning and the PXP model was to our knowledge never explicitly stated, so we will briefly explain it here. This mapping is valid in the regime $U \approx 2\delta \gg J$ and at filling factor $\nu = 1/2$.

When $U \approx 2\delta \gg J$, the second-order process $101 \leftrightarrow 020$ becomes resonant. Nonzero tilt Δ makes other relevant second-order processes such as $100 \leftrightarrow 001$ off-resonant. In this regime and for odd system size L with filling factor $\nu = \frac{L+1}{2L}$, the effective Hamiltonian at second order of the model in Eq. (20) is fragmented. One of these fragments can be mapped to the PXP model up to some diagonal boundary terms. To find the corresponding state in PXP, one only needs to look at the “minus” sites. Doublons on these sites are mapped to

PXP excitations, as the resonant processes cannot create two doublons on two adjacent minus sites. Due to the nature of the resonant process they can never be singly-occupied, and empty minus sites are mapped to non-excited atoms. This means that the corresponding PXP model has length $N = \frac{L-1}{2}$, which is just the number of minus sites.

The Néel states $\bullet\circ\bullet\circ\dots\circ\bullet$ and $\circ\bullet\circ\bullet\dots\circ\bullet$ are then mapped to $02000200\dots02001$ and $100200020\dots0020$ respectively, while $101010\dots101$ corresponds to the fully polarized state $\circ\circ\circ\dots\circ\circ\circ$.

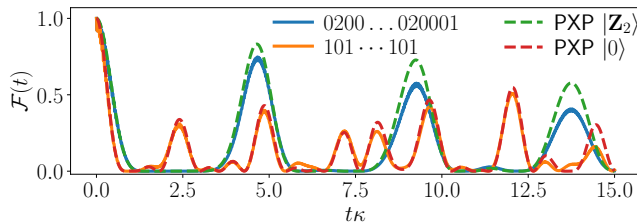


FIG. 7. Time evolution of the fidelity for tilted Bose-Hubbard model with staggered detuning with $L = 13$, $U = 2\delta = 120$, $J = 1$ and $\Delta = 43.3$, and for the PXP model with $N = 6$. The constant κ is the effective hopping strength in each model (see text).

Fig. 7 shows the wave function fidelity over time for the model in Eq. (20) with $U=2\delta > \Delta \gg J$, and for the PXP model it can be mapped to. To directly compare the two models, we have rescaled the time axis by the constant κ , which takes the value $\sqrt{2}J^{(2)} = \sqrt{2} \times 4J^2U/(U^2-4\Delta^2)$ in the Bose-Hubbard model and Ω in the PXP model. The staggered Bose-Hubbard model oscillates between two product states, $02000200\dots02001$ and $100200020\dots0020$, which are the analogs of the Néel states in the PXP model. Overall, the dynamics is seen to be very similar in the two models, with the slight difference between the two being likely due to the boundary terms defined in Eq. (21) below.

To derive the mapping to the PXP model rigorously, we can separate the Hamiltonian in Eq. (20) as $\hat{H} = \hat{H}_0 - J\hat{V}$ and perform the Schrieffer-Wolff transformation [7]. Here \hat{H}_0 encompasses all the diagonal terms while \hat{V} simply corresponds to hopping, which assumes that $\delta, \Delta, U \gg J$. Furthermore, we will only focus on the regime $U = 2\delta$, in which case there are no first order terms. If U is close but not equal to 2δ , then the effective Hamiltonian at first order will contain diagonal terms proportional to $|U - 2\delta|$. Finally, we only focus on the connected component of the second order Hamiltonian that can be mapped to the PXP model, meaning that resonant processes like $02010 \leftrightarrow 11001$ are ignored as these configuration cannot appear in the Hilbert space component of interest.

In the relevant part of the Hilbert space, the only off-diagonal resonant process at second order is $101 \leftrightarrow 020$, which appears with a weight of $\sqrt{2}J^{(2)}$, where $J^{(2)} =$

$\frac{4J^2U}{U^2-4\Delta^2}$. There are also two allowed second-order diagonal processes in the bulk of the chain: $010 \leftrightarrow 010$ and $020 \leftrightarrow 020$. They have a respective weight of $J^{(2)}$ and $2J^{(2)}$. However, as creating a new doublon emptying two singly-occupied sites, the diagonal matrix elements do not change under the off-diagonal process. The only exception to this is hopping at the boundaries of the chain. For the leftmost site, only hopping to the right and then back is possible, leading to a contribution of $\frac{2J^2}{U-2\Delta}$ instead of $J^{(2)}$. For the rightmost site only hopping to the left is possible and the contribution is $\frac{2J^2}{U+2\Delta}$. This means that not all diagonal matrix elements are the same but they vary between $J^{(2)}N = \frac{L-1}{2}J^{(2)}$ and $(N+1)J^{(2)} = \frac{L+1}{2}J^{(2)}$. However the differences between the diagonal elements are $\mathcal{O}(1)$ and do not scale with L , so they become negligible for large system sizes. All together, the second order Hamiltonian can be mapped to the following model.

$$\hat{H}_{\text{eff},2} = J^{(2)}N + \sqrt{2}J^{(2)} \left[\hat{X}_1 \hat{P}_2 + \hat{P}_{N-1} \hat{X}_N + \sum_{j=2}^{N-1} \hat{P}_{j-1} \hat{X}_j \hat{P}_{j+1} \right] + \frac{2J^2}{U+2\Delta} \hat{n}_1 + \frac{2J^2}{U-2\Delta} \hat{n}_N, \quad (21)$$

with $J^{(2)} = \frac{4J^2U}{U^2-4\Delta^2}$, $N = \frac{L-1}{2}$, $\hat{n}_j = \frac{1+Z_j}{2}$, where Z denotes the usual Pauli z matrix [\hat{P}_j and \hat{X}_j were defined previously below Eq. (5)]. It is worth mentioning that for $U = 2\delta$, the third order effective Hamiltonian is identically zero due to the absence of diagonal elements in the perturbation V (which is simply the hopping) and the next correction only happens at fourth order.

V. EFFECT OF PERIODIC DRIVING ON \mathbb{Z}_2 SCARS

In this section we numerically explore the effect of driving on the stabilization of many-body scars and revival dynamics, both in the PXP and tilted Bose-Hubbard models.

A. Driven PXP model

Periodic driving has been shown to enhance and stabilize the revivals in the PXP model [12, 13]. The optimal driving frequency was found to be close to twice that of revivals in the pure PXP model without driving. We consider the following spatially-uniform cosine driving scheme which was also experimentally implemented in Ref. [12]

$$\hat{H}(t) = \sum_i \left(\Omega \hat{P}_{i-1} \hat{X}_i \hat{P}_{i+1} - \mu(t) \hat{n}_i \right), \quad (22)$$

$$\mu(t) = \mu_0 + \mu_m \cos(\omega t). \quad (23)$$

1 Here, μ_0 is the static detuning, μ_m modulation amplitude and ω driving frequency. For simplicity, when working with the PXP model, we impose periodic boundary conditions (PBC). We determine the optimal values of μ_0 and μ_m by scanning the parameter space for the highest time-averaged fidelity. To make sure we found the globally-optimal values of the driving parameters, we have also checked the results against the simulated annealing algorithm implemented in GNU Scientific Library.

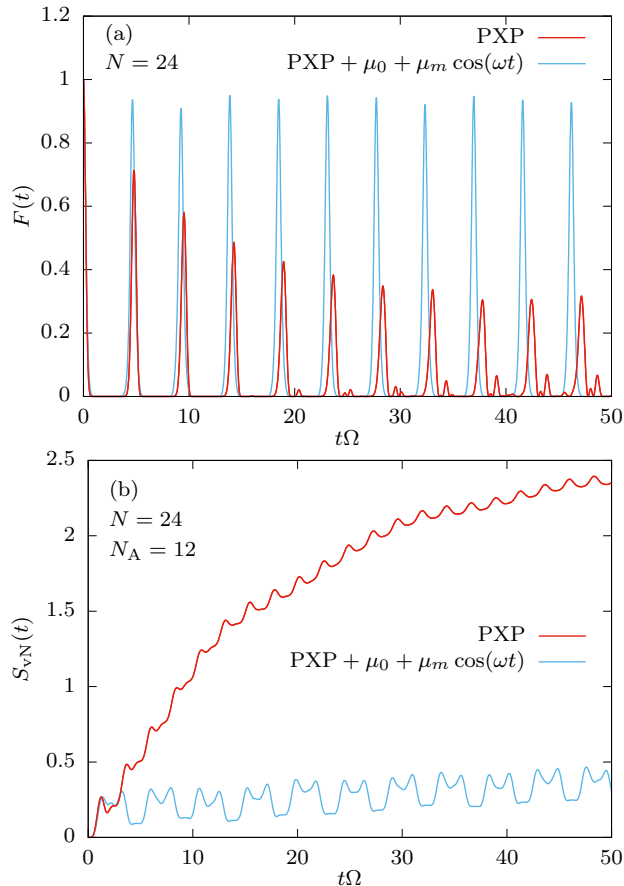


FIG. 8. Comparison of dynamics in the pure (red), and periodically driven PXP model (blue). System size $N = 24$, driving parameters $\mu_0/\Omega = 1.15$, $\mu_m/\Omega = 2.67$, $\omega/\Omega = 2.72$. (a) Fidelity. (b) Entanglement entropy for $N_A = 12$.

The evolution of quantum fidelity starting from the Néel state $|\mathbb{Z}_2\rangle = |\bullet\circ\bullet\circ\bullet\circ\dots\rangle$ can be seen in Fig. 8(a), both without driving (red) and driven with optimal driving parameters $\mu_0/\Omega = 1.15$, $\mu_m/\Omega = 2.67$ and $\omega/\Omega = 2.72$ (blue). Driving leads to high revivals whose amplitude remains close to 1 over very long times. Additionally, the driving also strongly suppresses the growth of entanglement entropy, as can be observed in Fig. 8(b).

In order to understand the mechanism of revival enhancement, in Fig. 9 we show the effects of periodic driving on the trajectory in the Hilbert space. The x and y axes in this figure are the expected numbers of excitations on the even and odd sublattice (normalized by

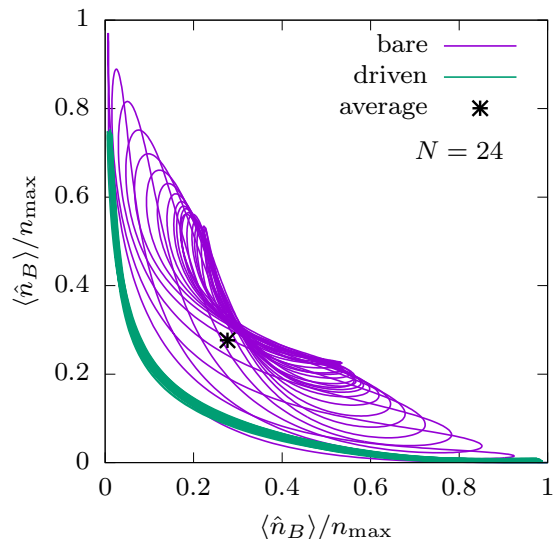


FIG. 9. Trajectory in the Hilbert space, represented by the expected numbers of excitations on the even and odd sublattices, $\langle \hat{n}_A \rangle$ and $\langle \hat{n}_B \rangle$, normalized by the maximal number of excitations $\hat{n}_{\max} = N/2$. Purple: no driving, $\mu(t) = 0$. The trajectory at first keeps returning to the vicinity of the Néel states, but then slowly relaxes towards the average value of $\langle \hat{n}_A \rangle$ and $\langle \hat{n}_B \rangle$. Green: driving with optimal parameters $\mu_0/\Omega = 1.15$, $\mu_m/\Omega = 2.67$ and $\omega/\Omega = 2.72$, results in dynamics that sharply concentrates around the trajectory and avoids thermalization.

the maximal number of excitations $n_{\max} = N/2$), $\langle \hat{n}_A \rangle$ and $\langle \hat{n}_B \rangle$ respectively. The two Néel states are located in the bottom right and top left corner of Fig. 9, while the polarized state $|\circ\circ\circ\dots\rangle$ is in the bottom left corner. The states on the main diagonal (except the Néel states) and in the triangle above it are forbidden due to the PXP constraints.

In the undriven case (purple), the trajectory at first oscillates between the Néel and anti-Néel states in the corners, while passing through a region with a lower number of excitations (bottom left). However, as the time progresses, the wavefunction starts to thermalize and the trajectory drifts towards towards the average numbers of excitations $(\langle \hat{n}_A \rangle, \langle \hat{n}_B \rangle) = (0.276, 0.276)$. When the driving is turned on (green), the trajectory continues to approximately repeat the first revival period in the undriven case and does not seem to thermalize even at very late times. In this way the revivals are stabilized and enhanced. Another effect of driving is that the overlap with the anti-Néel state is now lower, but its peaks do not decay with time.

Finally, in Fig. 10 we studied the Floquet modes of the driven PXP model. The Floquet modes are a generalization of eigenstates for periodic time-dependent Hamiltonians $\hat{H}(t + \frac{2\pi}{\omega}) = \hat{H}(t)$. Unlike the eigenstates, the Floquet modes evolve in time, but they are time-periodic with the same periodicity as the driven Hamiltonian, $\Phi_n(t + \frac{2\pi}{\omega}) = \Phi_n(t)$. We have computed all the Floquet modes $\Phi_n(t = 0)$ for the driven case by numerically con-

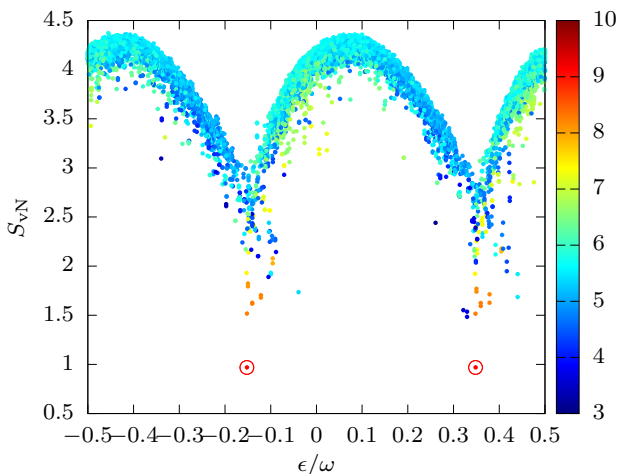


FIG. 10. Bipartite von Neumann entanglement entropies of all Floquet modes for the driven PXP model with driving parameters $\mu_0/\Omega = 1.15$, $\mu_m/\Omega = 2.67$ and $\omega/\Omega = 2.72$. System size $N = 20$, subsystem $N_A = 10$. The colour scale represents the expectation value of the total number of excitations for each state. The two Floquet modes which have the highest overlap with the Néel state are encircled in red. They have the lowest entanglement entropy and the highest number of excitations and their quasienergies are separated by $\omega/2$.

1 structing the evolution operator over one period $T = \frac{2\pi}{\omega}$,
 2 $\hat{U}(T)$, and diagonalizing it.

3 In Fig. 10 we plot the bipartite von Neumann entangle-
 4 ment entropies of all the Floquet modes for the optimal
 5 driving parameters. There are two symmetric ‘arcs’ in
 6 the entropy plot, which suggests that the Floquet Hamil-
 7 tonian might be fractured into two components. The
 8 expected numbers of excitations for each mode are rep-
 9 resented by different colours. The two lowest entropy
 10 modes have the highest overlap with the Néel state $|\mathbb{Z}_2\rangle$.
 11 One of them is approximately $\Phi_1(0) = (|\mathbb{Z}_2\rangle + |\mathbb{Z}'_2\rangle)/\sqrt{2}$
 12 and the other is close to $\Phi_2(0) = (|\mathbb{Z}_2\rangle - |\mathbb{Z}'_2\rangle)/\sqrt{2}$,
 13 while the quasienergy separation between them is $\Delta\epsilon =$
 14 $\epsilon_1 - \epsilon_2 \approx \omega/2$. This provides a simple explanation for the
 15 revival dynamics starting from the Néel state, as will be
 16 outlined below.

Let us assume that the two idealized states $\Phi_1(0)$ and $\Phi_2(0)$ are indeed Floquet modes. The initial state $|\mathbb{Z}_2\rangle$ will then be a superposition of only these two modes

$$\psi(0) = \frac{1}{\sqrt{2}}\Phi_1(0) + \frac{1}{\sqrt{2}}\Phi_2(0) \quad (24)$$

and will evolve as

$$\begin{aligned} \psi(t) &= \frac{1}{\sqrt{2}}e^{-i\epsilon_1 t}\Phi_1(t) + \frac{1}{\sqrt{2}}e^{-i\epsilon_2 t}\Phi_2(t) = \\ &= \frac{1}{\sqrt{2}}e^{-i\epsilon_1 t}(\Phi_1(t)) + e^{i\Delta\epsilon t}\Phi_2(t). \end{aligned} \quad (25)$$

17 After one driving period, the two Floquet modes will re- 35
 18 turn to their initial states, but the relative phase will be 36

19 $e^{i\frac{\omega}{2}\frac{2\pi}{\omega}} = e^{i\pi} = -1$. The wavefunction after one period
 20 will therefore be in the anti-Néel state (with an unim-
 21 portant phase prefactor), $\psi(T) = e^{-i\epsilon_1 T}|\mathbb{Z}'_2\rangle$. It will take
 22 two driving periods for the relative phase to again become
 23 $+1$ and the wavefunction to return to the initial $|\mathbb{Z}_2\rangle$
 24 state. This is the origin of the period doubling (subhar-
 25 monic response to periodic driving) which was observed
 26 in previous works [12].

27 We note that the period doubling will disappear if we
 28 resolve the translation symmetry and work only in the
 29 $k = 0$ momentum subspace. The initial state $(|\mathbb{Z}_2\rangle +$
 30 $|\mathbb{Z}'_2\rangle)/\sqrt{2}$ will in that case have high overlap with only a
 31 single Floquet mode and will trivially oscillate with the
 32 same frequency as the periodic drive.

B. Driving the tilted 1D Bose-Hubbard model

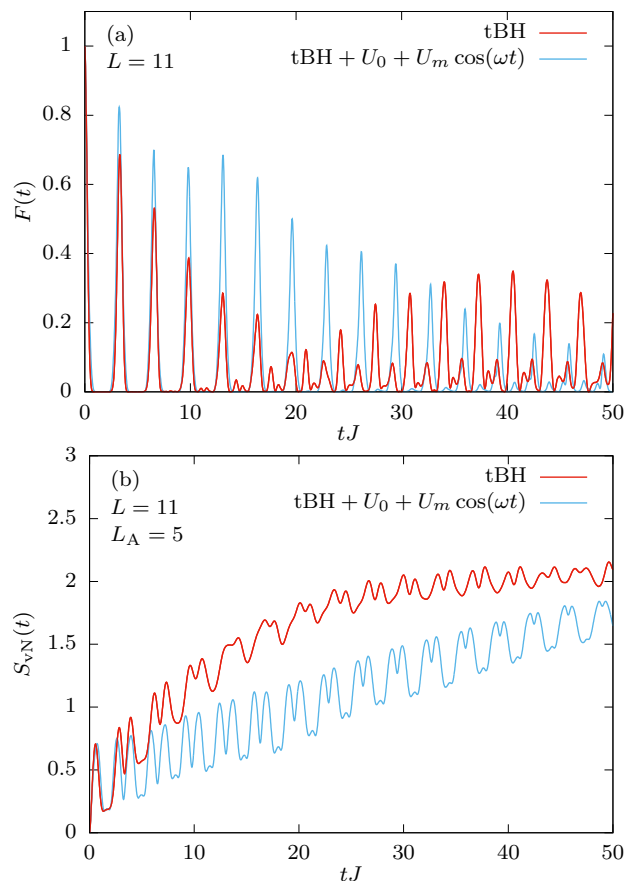


FIG. 11. Comparison of the dynamics in the tilted Bose-Hubbard model without (red) and with periodic driving (blue). System size $L = 11$, maximally 3 particles per site, $J = 1$, $\Delta = 16$, driving parameters $U_0 = 1.85$, $U_m = 3.71$, $\omega = 3.85$. (a) Fidelity. (b) Entanglement entropy for subsystem size $L_A = 5$ sites.

As the tilted Bose-Hubbard model can be mapped to the PXP model in the $U \approx \Delta \gg J$ limit, see Section I, we also expect to be able to enhance many-body scar-

ring via periodic modulation of the term corresponding to the number of excitations. In the Bose-Hubbard case such a term is conveniently provided by the on-site interaction strength U . However, we cannot use periodic boundary conditions due to the linear tilt which would be discontinuous at the boundary. We therefore consider the Bose-Hubbard model with open boundary conditions and periodically modulate the interaction strength $U(t)$:

$$\hat{H}(t) = -J \sum_{i=1}^{L-1} (\hat{b}_i^\dagger \hat{b}_{i+1} + \hat{b}_{i+1}^\dagger \hat{b}_i) + \frac{U(t)}{2} \sum_{i=1}^L \hat{n}_i (\hat{n}_i - 1) + \Delta \sum_{i=1}^L i \hat{n}_i, \quad (26)$$

with the driving given by

$$U(t) = \Delta + U_0 + U_m \cos(\omega t). \quad (27)$$

The driving parameters, U_0 , U_m and ω , are the static detuning and the modulation amplitude of the interaction strength and the driving frequency, respectively.

The modulation of interaction strength indeed leads to enhanced revivals in the Bose-Hubbard model, see Fig. 11. In particular, the slope of entanglement growth is significantly reduced, with scarred oscillations becoming more pronounced. However, in local observables, such as the density of doublons, the effects of driving are less striking than in the pure PXP model. The reason for more modest enhancement of revivals in the Bose-Hubbard model is the competition between stabilization of revivals within the PXP subspace and the processes which destroy the mapping to PXP model, such as the terms creating 3 or more bosons on a site. Additionally, the optimal driving parameters are not the same as those for the PXP model (up to the trivial rescaling by $\Omega = \sqrt{2}J$ to match the normalization of off-diagonal matrix elements). Increasing the tilt parameter Δ brings the tilted Bose-Hubbard model closer to the PXP model, but it is still necessary to perform a separate optimization of driving parameters.

VI. QUANTUM MANY-BODY SCARS IN THE POLARIZED STATE

In the main text we reported the observation of many-body scarring associated with the state that contains no doublons, $|111\dots\rangle$, or equivalently the fully-polarized state $|\circ\circ\circ\dots\rangle$ in the PXP model. In this section we provide extensive theoretical evidence for many-body scarring in the polarized state. While the polarized state does not exhibit many-body scarring in the pure PXP model, consistent with previous work [14], it does display weak signatures of non-ergodicity in local observables for sufficiently small systems. In this section, we show that static detuning and its periodic modulation can be used to stabilize the scarring from this initial state. As we will

demonstrate below, the many-body scarring in the polarized state is distinct from the previously studied ‘‘dynamical freezing’’ regime associated with $|\circ\circ\circ\dots\rangle$ state in the PXP model driven by a square pulse protocol [15].

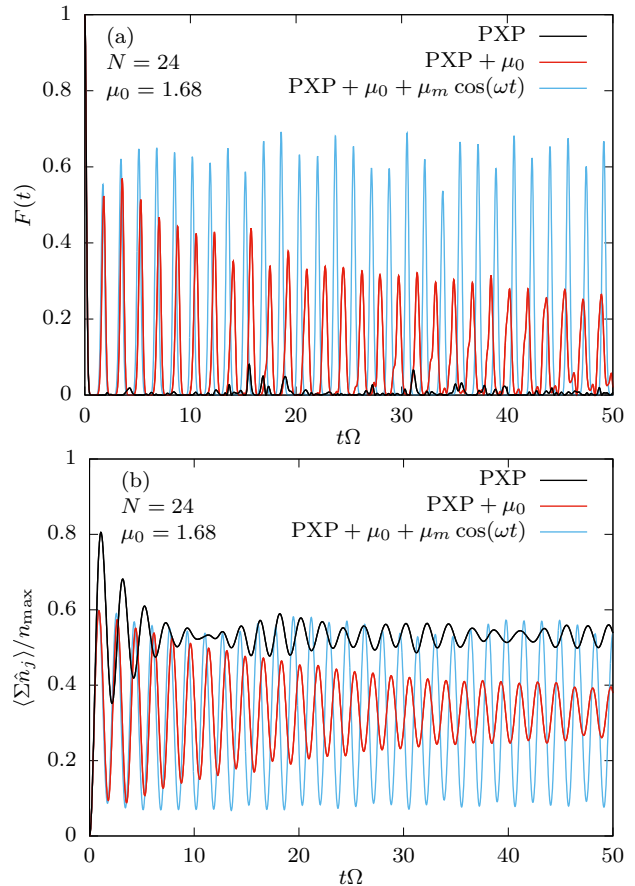


FIG. 12. Comparison of dynamics from the polarized state in the pure PXP model (black), with static detuning only (red), and with both static detuning and periodic driving (blue). System size $N = 24$, driving parameters $\mu_0/\Omega = 1.68$, $\mu_m/\Omega = -0.50$, $\omega/\Omega = 3.71$. (a) Fidelity. (b) Expected total number of excitations normalized by the maximal number of excitations $n_{\max} = N/2$.

A. Pure PXP model

The polarized state $|\circ\circ\circ\dots\rangle$ is expected to thermalize in the pure PXP model. Nevertheless, the state exhibits some signatures of non-ergodic dynamics in smaller system sizes, such as oscillations in the expectation values of certain local observables. For example, as shown by the black lines in Figs. 12(a) and (b), even though there are no significant revivals in wave function fidelity, some oscillations in the number of excitations are still visible.

A closer look at the eigenstates of the PXP Hamiltonian and their overlap with the polarized state reveals the underlying reason for this behaviour, see Fig. 13. In Fig. 13(a) we plot the overlap of all PXP eigenstates with

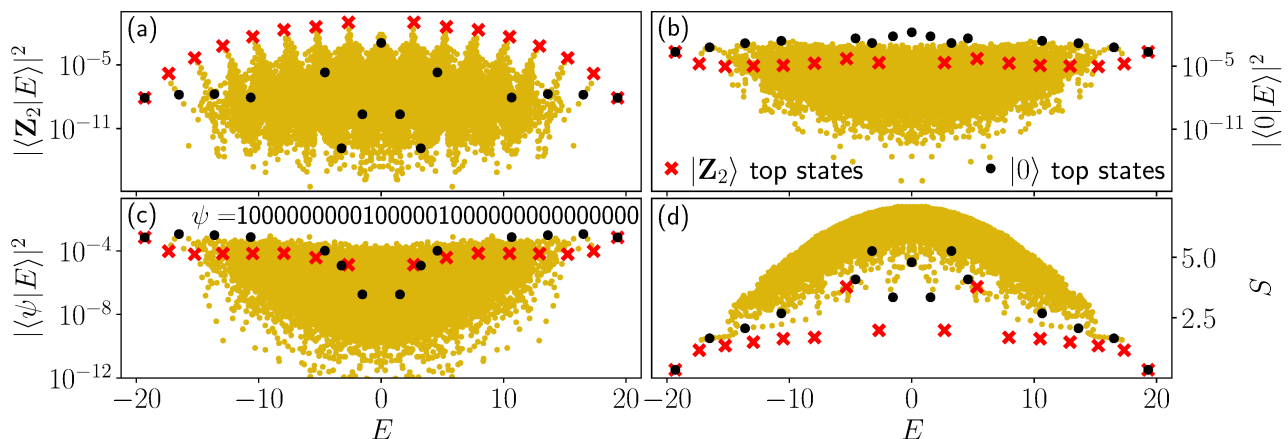


FIG. 13. PXP eigenstates, system size $N = 32$, symmetry sector $\{k = 0, p = 1\}$. Overlap with (a) Néel state. (b) polarized state. (c) randomly chosen state. (d) Bipartite entanglement entropies of all eigenstates. The highest-overlap eigenstates in their energy window are marked by red crosses for the Néel state and by black dots for the polarized state.

1 the Néel state, showing the well known band [5] of scarred
 2 eigenstates marked by the red crosses and corresponding
 3 tower structures. In contrast, there is no such band of
 4 high-overlap eigenstates for a randomly chosen state, see
 5 Fig. 13(c). The polarized state is between these two cases,
 6 as can be observed in Fig. 13(b). Although there is no
 7 well defined band of scarred eigenstates as for the Néel
 8 state, there is still a number of unusually high-overlap
 9 eigenstates which are marked by the black dots. Finally,
 10 in Fig. 13(d) we show the entanglement entropies of all
 11 eigenstates. The lowest-entropy eigenstates are the Néel
 12 state scars (red crosses), but the eigenstates with the
 13 highest overlap with the polarized state (black dots) also
 14 have lower than average entanglement entropies. Thus,
 15 we conclude that the polarized state is poised to develop
 16 many-body scarring by a suitable perturbation of the
 17 PXP model. We next show that this can be achieved
 18 by applying static detuning.

B. Static detuning in the PXP model

The addition of a static detuning term

$$\hat{H}(\mu_0) = \hat{H}_{\text{PXP}} + \mu_0 \sum_j \hat{n}_j \quad (28)$$

21 results in the appearance of a band of atypical eigenstates
 22 with high overlap with the polarized state, as can be ob-
 23 served in Fig. 14. The band is still not well separated
 24 from the bulk at lower values of μ_0/Ω , see Figs. 14(a) and
 25 (b). At larger values of μ_0/Ω , the energy spectrum starts
 26 to split into disconnected bands, as shown in Fig. 14(d).
 27 We are interested in the intermediate regime shown in
 28 Fig. 14(c), $\mu_0/\Omega \approx 1.68$, where there is a clearly visi-
 29 ble band of scarred states, but the bulk of the energy
 30 spectrum is still continuous.

32 In addition to having the highest overlap with the po-
 33 larized state, the special states are also approximately

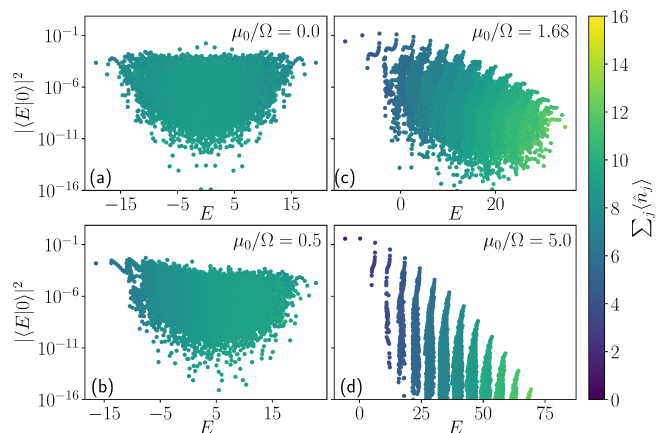


FIG. 14. Overlap between the polarised state and the PXP eigenstates in the symmetry sector $\{k = 0, p = 1\}$ for $N = 32$. Each subfigure corresponds to a different value of the static detuning, and the color indicates the expectation value of the number of excitations for each eigenstate.

34 equidistant in energy and have lower entanglement en-
 35 tropy than most other eigenstates. These are all paradig-
 36 matic properties of quantum many-body scars. However,
 37 one striking difference compared to the Néel state scars
 is that the highest-overlap states are not concentrated in
 the middle of the spectrum. Instead, most of them are lo-
 cated at one edge of the energy spectrum, but the band of
 atypical states still continues well into the higher energy
 densities, see Fig. 14(c). The fact that special eigenstates
 are biased towards one end of the spectrum is expected
 since the detuning potential breaks the particle-hole sym-
 metry of the PXP Hamiltonian [6].

This emergence of scarred eigenstates significantly af-
 fects the revival dynamics, as illustrated in Figs. 12 and
 15. For the Néel state in Fig. 15(a), the detuning mono-
 tonically destroys the revival, until we reach the regime

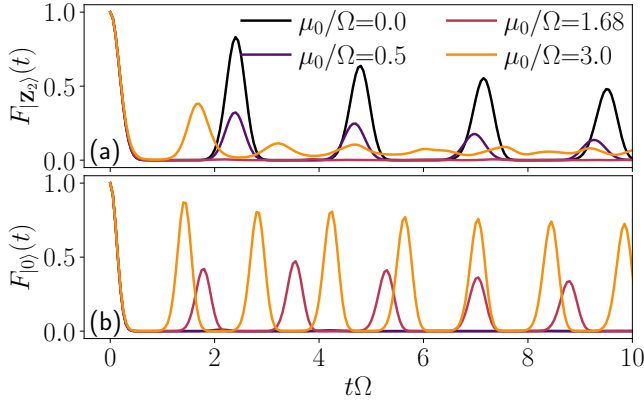


FIG. 15. Revival fidelity for the Néel and polarised states in the symmetry sector $\{k = 0, p = 1\}$ for $N = 32$. (a) Néel state. (b) polarized state. At low detuning only the Néel states revives while in for $\mu_0/\Omega \gg 1$ both states do. However in the intermediate regime $\mu_0/\Omega \approx 1$ only the polarised states has revivals while the Néel state thermalises like the other product states.

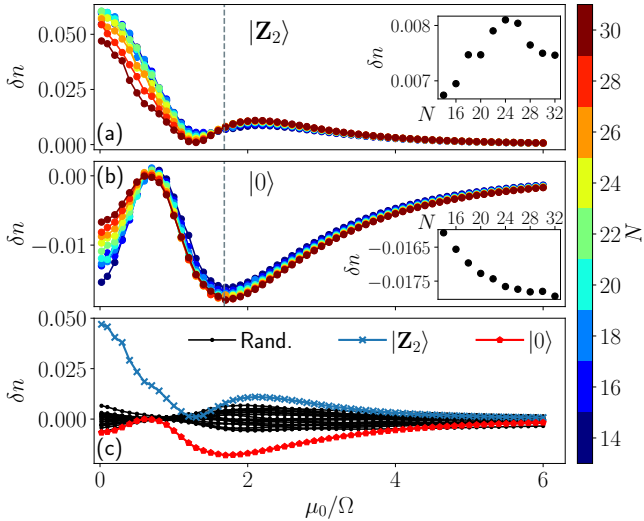


FIG. 16. Difference of expectation value between the diagonal and canonical ensemble for the operator $\frac{1}{N} \sum_j \hat{n}_j$ in the PXP model. (a) Néel state. (b) polarized state. (c) comparison of different states for $N = 30$. The color scale in (a) and (b) corresponds to the system size N , while the insets show the results for various N with μ_0/Ω fixed to 1.68 (along the grey dashed line).

of very large detuning $\mu_0 \gtrsim 3$ which places the Néel state in its own fragment of the Hilbert space. By contrast, for the polarized state in Fig. 15(b) we see the revivals start to emerge at moderate detuning $\mu_0/\Omega \approx 1$. The frequency of the revival is found to match the energy separation between the scarred states in Fig. 14(c). The oscillations in the number of excitations are also enhanced and their frequency has changed to the frequency of fidelity revivals. This is the regime that corresponds to the

many-body scarring observed in experiment. We note that the revivals from the polarized state also persist in the trivial large-detuning limit ($\mu_0 \gtrsim 3$) where the polarized state is effectively in its own fragment of the Hilbert space, similar to the Néel state.

The addition of detuning not only affects the short-time dynamics, but also *infinite-time* expectation values. After a quench, the value of any observable will reach the value predicted by the diagonal ensemble $O_d = \sum_{i,j} O_{i,j} \delta_{i,j} c_j c_i^*$, where $O_{i,j} = \langle E_i | O | E_j \rangle$ and $c_i = \langle E_i | 0 \rangle$. However we also expect the observable to thermalize towards the value predicted by the canonical ensemble $O_{th} = \text{Tr} [\hat{\rho}_{th} \hat{O}]$, where $\hat{\rho}_{th} = \frac{1}{\mathcal{Z}} e^{-\beta \hat{H}}$ with $\mathcal{Z} = \text{Tr} [e^{-\beta \hat{H}}]$ and β the inverse temperature. Note that we also restrict \hat{H} to the symmetry sector invariant under translation and spatial inversion as it is the only one compatible with the $|0\rangle$ state. A large difference between the predictions of these two ensembles for a given initial state is an indicator of the violation of the Eigenstate Thermalization Hypothesis [16, 17]. For the PXP model we will use the operator $\hat{n} = \frac{1}{N} \sum_j \hat{n}_j$, which counts the average number of excitations in the system [18], and denote the difference between the ensemble predictions by δn . The Néel state is most athermal at zero detuning, while the peak for the polarised state occurs around $\mu_0/\Omega = 1.7$, see Fig. 16. For larger values of the detuning these two states become respectively the topmost and ground states, meaning that the temperature is $\pm\infty$ and both ensembles agree exactly.

C. Periodic driving in the PXP model

Finally, in order to stabilize revival and many-body scarring in the polarized state at *late* times, we need to modulate the detuning amplitude, in addition to the static detuning. Using the same driving protocol as for the Néel state in Eq. (23), we can enhance and stabilize the revivals from the polarized state at late times – see Fig. 12 (blue lines). The optimal driving frequency is found to be close to the frequency of revivals in the undriven case with static detuning.

In Fig. 17 we plot the entanglement energies of all the Floquet modes $\Phi_n(t = 0)$ for the optimal driving parameters. As in Fig. 10, the colour scale represents the expected number of excitations for each mode. The translational symmetry is now resolved and we show only the modes inside the $k = 0$ momentum subspace. There is a single mode that has high overlap with the polarized state, which explains the revival dynamics in Figs. 12 and 15(b). Note that there is no period doubling in this case.

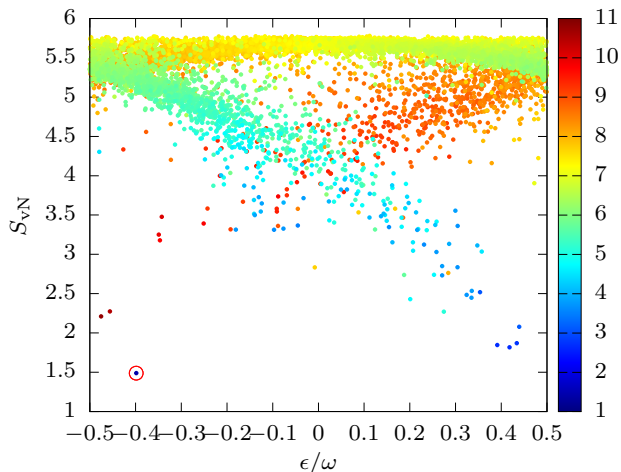


FIG. 17. Bipartite von Neumann entanglement entropies of all Floquet modes for $\mu_0/\Omega = 1.68$, $\mu_m/\Omega = -0.50$ and $\omega/\Omega = 3.71$. System size $N = 26$, subsystem $N_A = 13$, symmetry sector $k = 0$. The colour scale represents the expectation value of the total number of excitations for each state. The Floquet mode with the highest overlap with the polarized state is encircled in red. This mode has the lowest entanglement entropy and the lowest number of excitations.

D. Detuning and periodic driving in the tilted Bose-Hubbard model

Finally, we confirm that our conclusions about many-body scarring associated with the polarized state also hold in the full tilted Bose-Hubbard model in the regime $U \approx \Delta$, where we expect the effective description to be close to the PXP model. We will show that the driving leads to a strong suppression of entanglement growth and makes off-resonant the processes that cause leakage out of the PXP subspace.

In Fig. 18 we compare the dynamics at the resonance $U = \Delta$ (black lines, corresponding to the pure PXP model), at $U = \Delta + U_0$ (red lines, corresponding to the PXP model with static detuning), and for $U(t) = \Delta + U_0 + U_m \cos(\omega t)$ (blue lines, corresponding to the periodically driven PXP model). Due to the very fast growth of the Hilbert space size, we restrict the maximal number of bosons per site to 3. The results are consistent with those for the PXP model shown in Fig. 12. Note that the frequency of fidelity revivals in Fig. 18(a) is the frequency of PXP revivals multiplied by a factor of $\sqrt{2}$ which comes from the off-diagonal matrix elements in the Bose-Hubbard model. The expected number of doublons, which is related to the number of PXP excitations is shown in Fig. 18(b).

The growth of entanglement entropy is suppressed by the addition of static detuning and even more by periodic driving, see Fig. 18(c). There are two factors that contribute to this behaviour. One is the dynamics inside the PXP subspace. The other is related to the leakage out of this subspace, which is represented by the number of

sites with 3 particles in Fig. 18(d). The static detuning by itself significantly decreases this quantity, while the periodic driving does not seem to result in a substantial further improvement for the polarized state.

VII. OTHER QUANTUM MANY-BODY SCARRED STATES

In addition to the Néel state and the polarized state, we also find other initial states which revive in the PXP model with static detuning, Eq. (28). These initial states are the ground states of $\hat{H}(\mu_i)$ and they exhibit revivals when the detuning is quenched to a different value, $\hat{H}(\mu_i) \rightarrow \hat{H}(\mu_f)$. This setup generalizes the quench protocols studied in the main text. For example, setting $\mu_i \rightarrow -\infty$, the ground state is simply the Néel state and then quenching to $\mu_f = 0$ (pure PXP model) leads to the appearance of \mathbb{Z}_2 quantum many-body scars. Similarly, if we set $\mu_i \rightarrow \infty$ then the ground state is the $|0\rangle$ state and quenching to $\mu_f = 1.68\Omega$ also leads to scarring, as shown in the main text.

However, we observe similar scarring phenomenology in a larger set of initial conditions by varying the parameters μ_i and μ_f . Unlike the Néel state and the polarized state, the ground states of $\hat{H}(\mu_i)$ are far from product states for $|\mu_i| < 2$. However, they also have low entanglement and can be prepared experimentally. In Fig. 19 we illustrate this with an example for $\mu_i = -0.76\Omega$ and $\mu_f = 1.6\Omega$. For this set of parameters, we recover a similar scarring phenomenology as shown in the main text for the polarized state with $\mu_0 = 1.68$. However, we stress that the initial state considered here, i.e., the ground state of $\hat{H}(\mu_i)$, is now far from both the Néel and polarized states (the overlap with these states is on the order 10^{-5}). We emphasize that these values of μ are not fine tuned, and we find large regions of μ_i and μ_f leading to scarring.

In Fig. 19 (a) we recover a dynamics close to what could be observed for the polarized state with $\mu = 1.68\Omega$. During the evolution, the state periodically transfers to the polarized state and then returns to itself. The frequency of revivals is approximately the same as that for the polarized state evolved with the same static detuning μ_f , but the revivals are more prominent. The overlap of the $\hat{H}(\mu_i)$ ground state with all the eigenstates of $\hat{H}(\mu_f)$ is shown in Fig. 19(b). Comparing with the top states having overlap with the polarized state at the same value μ_f (red crosses) we see a similar pattern. More than that, the same atypical eigenstates have a high overlap for both states, but the phase is different in the two cases. This is similar to what is observed with the Néel state and its translated version for $\mu_f = 0$. Both have the same overlap magnitude with each eigenstate, but the phases are different.

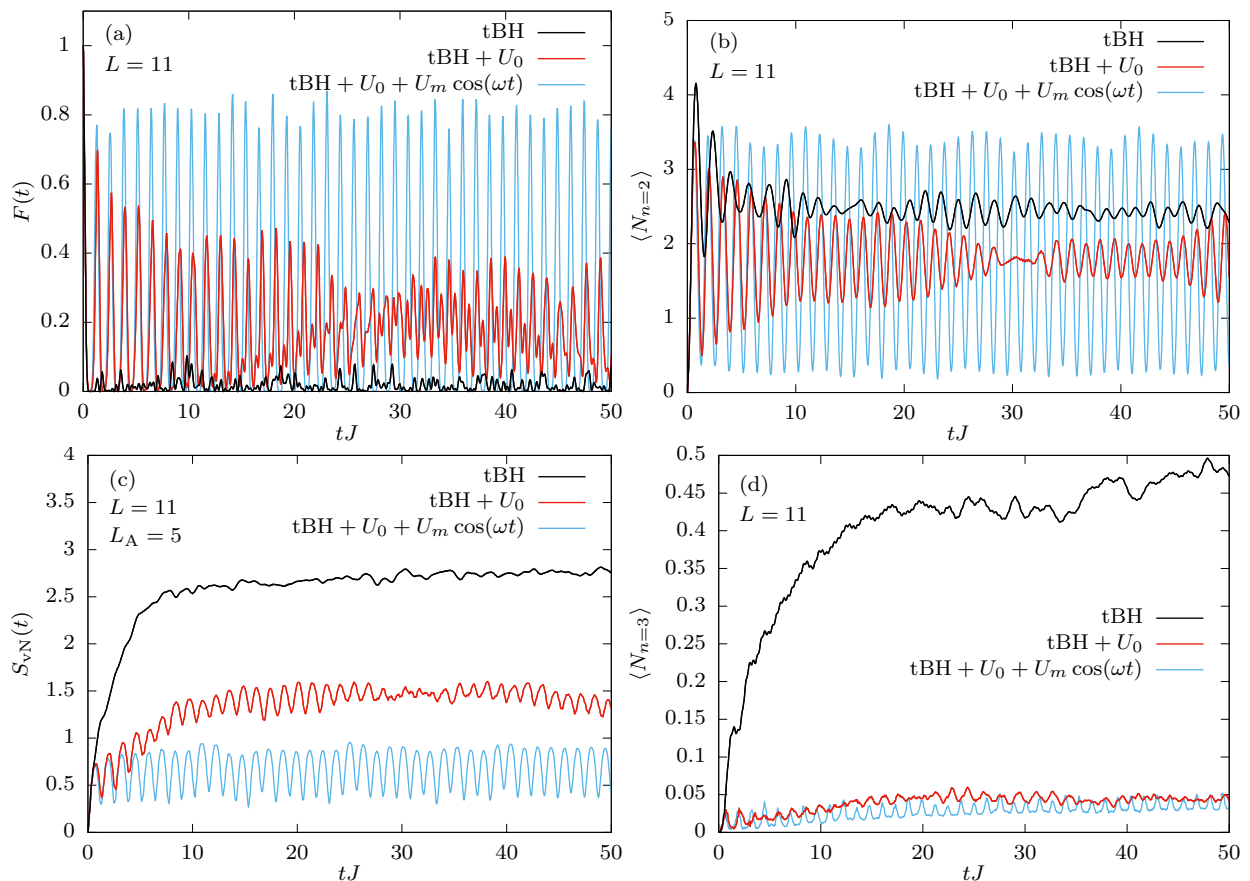


FIG. 18. Comparison of dynamics in the tilted Bose-Hubbard model (black), with static detuning only (red), and with both static detuning and periodic driving (blue). System size $L = 11$, maximally 3 particles per site, $J = 1$, $\Delta = 16$, driving parameters $U_0 = -2.38$, $U_m = 1.54$, $\omega = 4.90$. (a) Fidelity. (b) Expected total number of doublons $N_{n=2}$. (c) Entanglement entropy for subsystem size $L_A = 5$. (d) Expected total number of sites with three particles $N_{n=3}$ (indicates the leakage from the PXP subspace).

VIII. EFFECT OF DETUNING ON THE SPECTRAL STATISTICS OF THE PXP MODEL

In this section we show that the addition of finite detuning to the PXP model does not make this model integrable. We study the energy level spacings $s_n = E_{n+1} - E_n$, which we normalize to have $\langle s_n \rangle = 1$. For an integrable model, $\{s_n\}$ should follow the Poisson distribution, while for a chaotic model we expect to see the Wigner-Dyson distribution. A convenient way to probe level statistics is by computing the so-called $\langle r \rangle$ parameter [19], defined as the average of level spacing ratios:

$$r_n = \frac{\min(s_n, s_{n-1})}{\max(s_n, s_{n-1})}. \quad (29)$$

For the Poisson statistics, we expect $\langle r \rangle \approx 0.39$, while $\langle r \rangle \approx 0.53$ for Wigner-Dyson. In Fig. 20 we show that $\langle r \rangle$ tends towards 0.53 as N increases, for all values of μ . In general, as μ becomes larger, the convergence is slower because the detuning approximately conserves the number of excitations. Beyond that, one can also notice two dips in $\langle r \rangle$ at $\mu = 0$ and $\mu \approx 1.6$, hinting that near these

values PXP is close to another integrable model. For pure PXP this had been noted and previously investigated with various other perturbations [20].

The full distribution of the s_n is shown in Fig. 21 for $\mu = 0, 1$, and 1.6829 for $N=32$ spins. In all cases, we see that the distribution resembles Wigner-Dyson, even though in the last case it is skewed towards zero.

In conclusion, for any finite value of μ , the PXP model is non-integrable and its level statistics follow the Wigner-Dyson distribution in a large enough system size. Interestingly, the level statistics suggests a proximity to an integrable model at the points where we find good revivals due to scars: at $\mu = 0$ for the Néel state and near $\mu = 1.68$ for the polarized state. These results are in accordance with the discrepancies observed between the diagonal and canonical ensembles in Fig. 16.

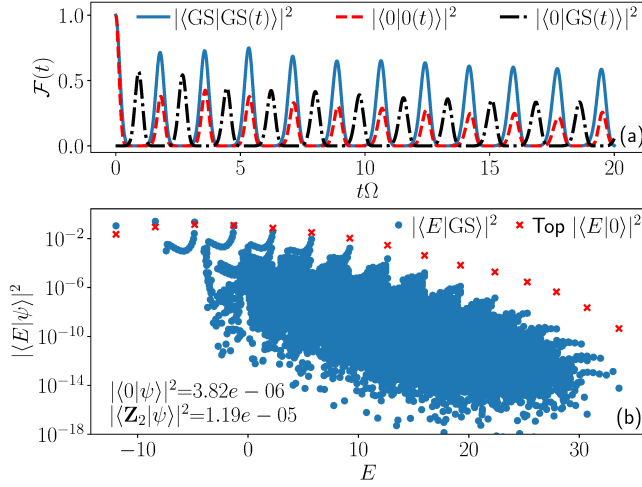


FIG. 19. Emergence of many-body scarring by quenching the PXP model from $\mu_i = -0.76\Omega$ to $\mu_f = 1.6\Omega$ for $N = 32$ spins in the $k=0$, $p=1$ symmetry sector. The dynamics is very similar to that of the polarized state at the same μ_f , with the overlap between the two suggesting that state transfer happens between them. The overlap between these two states and the eigenstates of $\hat{H}(\mu_f)$ also shows similar tower structures.

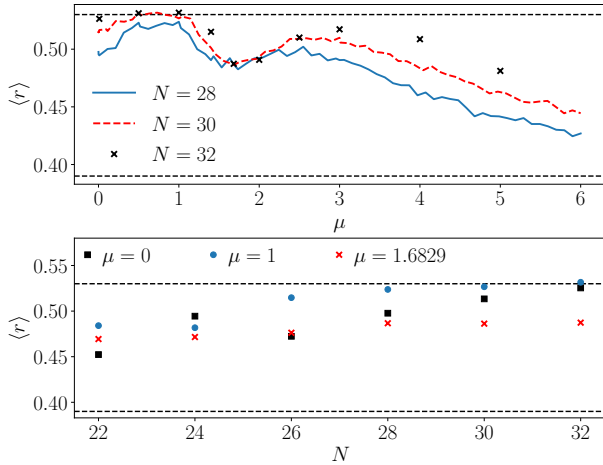


FIG. 20. $\langle r \rangle$ for the PXP model with various system sizes N and detuning μ . For all values of μ shown, the spectral statistics flows towards Wigner-Dyson value, as the $\langle r \rangle$ parameter increases with system size. However the convergence is slower near $\mu = 0$, $\mu = 1.68$, and in general as μ becomes larger.

IX. SYSTEM-SIZE SCALING OF THE REVIVAL FIDELITY

An important question concerns the stability of revivals in the thermodynamic limit. In particular, due to the cost of non-linear optimization, the driving parameters were obtained in relatively small systems, therefore it needs to be checked whether the same parameters work as well in large systems. For the calculations in this sec-

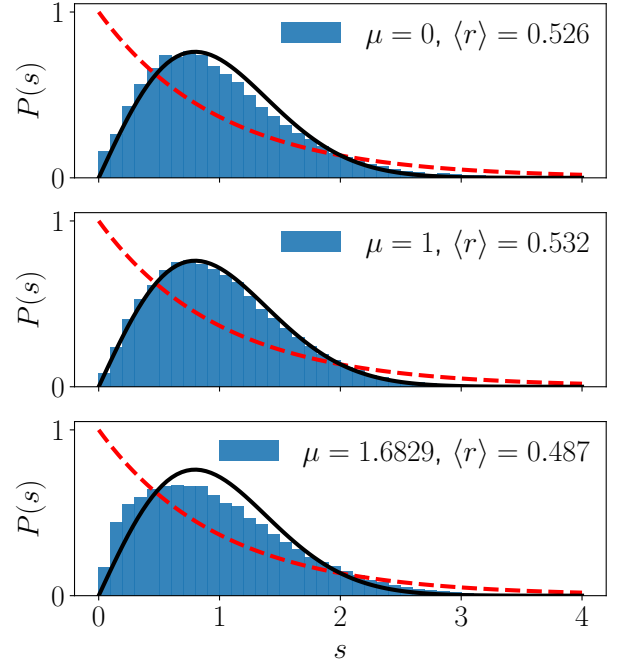


FIG. 21. Distribution of the level spacings after spectrum unfolding for the PXP model with $N=32$. The solid black line corresponds to the Wigner-Dyson distribution and the dashed red line to Poisson. In all cases the distribution is close to Wigner-Dyson, even though for $\mu = 1.6829$ it is skewed towards $s = 0$.

tion, we perform time evolution in large systems using the TEBD algorithm implemented in TenPy package [9], as explained in Sec. II.

Figs. 22 and 23 show the system size scaling of the first three revival peaks for different initial states, both with and without driving. The results were obtained from numerical simulations of the tilted Bose-Hubbard model, Eq. (26), with open boundary conditions, $\Delta/J = 16$, and maximally 3 particles per site. This particle number limit is a reasonable assumption since the periodically driven interaction strength $U(t) = \Delta + U_0 + U_m \cos(\omega t)$ is large compared to the hopping amplitude J . In the case of global fidelity $F(t)$, we plot the so-called fidelity density $-\ln(F(nT))/L$, where T is the revival period and $n \in \{1, 2, 3\}$. The single-site fidelity $\mathcal{F}_{(1)}(t)$ is a local quantity, so it does not need to be rescaled by the system size L . We therefore simply plot the peak heights $\mathcal{F}_{(1)}(nT)$.

For the Néel state $2020 \dots 20$, the fidelity density is expected to converge to a constant value in the limit of large L . This is consistent with our results in Fig. 22(a), where we plot the fidelity density after one, two and three driving periods. The driving parameters are the same for all system sizes, $\omega = 3.85$, $U_0 = 1.85$ and $U_m = 3.71$. Due to the minus sign in the definition, lower fidelity density corresponds to higher revival peaks and vice versa. As can be observed in Fig. 22(a), periodic driving leads to

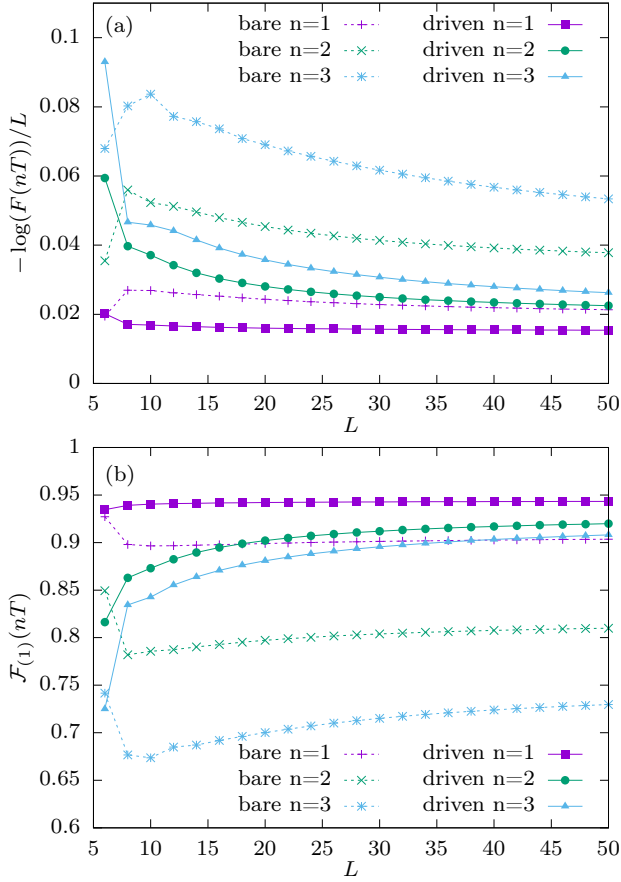


FIG. 22. System size scaling of the first three revival peaks for the Néel state $|\mathbb{Z}_2\rangle = |2020\dots 20\rangle$. Driving parameters $\omega = 3.85$, $U_0 = 1.85$, $U_m = 3.71$. Dashed lines correspond to the bare case and the solid lines to the driven case. (a) Fidelity density. (b) Single-site fidelity.

1 increased revivals over a broad range of system sizes and
 2 there is no indication that this will change for $L > 50$.
 3 The revivals are decaying with time, but the decay is
 4 significantly slower when the driving is turned on. We
 5 can thus conclude that periodic driving with these pa-
 6 rameters both enhances and stabilises the revivals, even
 7 in relatively large systems.
 8 The scaling of the single-site fidelity can be observed in
 9 Fig. 22(b). This experimentally measurable quantity rep-
 10 represents a tight upper bound for the global fidelity when
 11 the system is initialized in a product state, see Section III.
 12 The results are similar to those for the global fidelity. In
 13 all cases, the revival heights are rapidly converging to-
 14 wards a constant value. Again, the revivals in driven
 15 systems are significantly higher than those without driv-
 16 ing and the difference between them increases with time.
 17 The effects of periodic driving are even more striking
 18 with the polarized state $111\dots 111$ as the initial state, as
 19 shown in Fig. 23. There are no notable revivals in global
 20 fidelity when the driving is turned off. The dashed lines
 21 in Fig. 23(a) correspond to irregular minor local maxima
 22 which are present in smaller systems. Even these local

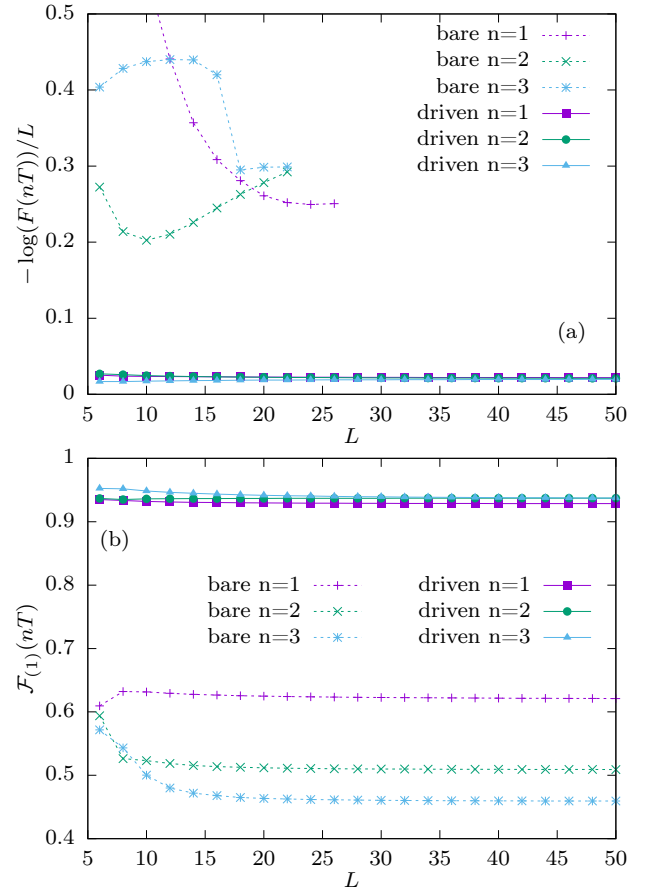


FIG. 23. System size scaling of the first three revival peaks for the polarized state $|111\dots 111\rangle$. Driving parameters $\omega = 4.90$, $U_0 = -2.38$, $U_m = 1.54$. Dashed lines correspond to the bare case and the solid lines to the driven case. Data points are missing in cases where there are no local maxima. (a) Fidelity density. (b) Single-site fidelity.

maxima disappear with increasing system size, which ex-
 11 plains why some data points are missing. In contrast,
 12 driving with parameters $\omega = 4.90$, $U_0 = -2.38$ and
 13 $U_m = 1.54$ produces very high revivals which do not de-
 14 cay, either with time or with system size. The single-site
 15 fidelity tells a similar story, see Fig. 23(b), however in this
 16 case there are revivals even in the absence of driving, con-
 17 sistent with dynamics of local observables in Fig. 12(b).

Finally, we note that the Néel and polarized states are
 the only two initial product states for which we were able
 to find optimal driving parameters that lead to robust
 revivals at late times. This is true both for the tilted
 Bose-Hubbard model, Eq. (26) in the $\Delta \approx U$ regime,
 and for the PXP model with a spatially uniform driv-
 ing protocol. For other initial states, such as \mathbb{Z}_4 state
 with an excitation on every fourth site or, equivalently,
 20112011 \dots 2011 in the tilted Bose-Hubbard model, it is
 possible to stabilize a small number of revivals at short
 times. In contrast to the Néel and polarized states, these
 revivals are found to decay quickly with time as well as

1 with system size.

-
- 2 [1] I. Lesanovsky and H. Katsura, *Phys. Rev. A* **86**, 041601 25
3 (2012). 26
- 4 [2] P. Fendley, K. Sengupta, and S. Sachdev, *Phys. Rev. B* 27
5 **69**, 075106 (2004). 28
- 6 [3] S. Sachdev, K. Sengupta, and S. M. Girvin, *Phys. Rev.* 29
7 **B 66**, 075128 (2002). 30
- 8 [4] K. Sengupta, “Phases and dynamics of ultracold bosons 31
9 in a tilted optical lattice,” (2021), [arXiv:2109.02657](https://arxiv.org/abs/2109.02657) 32
10 [[cond-mat.quant-gas](https://arxiv.org/abs/2109.02657)]. 33
- 11 [5] C. J. Turner, A. A. Michailidis, D. A. Abanin, M. Serbyn, 34
12 and Z. Papić, *Nature Physics* **14**, 745 (2018). 35
- 13 [6] C. J. Turner, A. A. Michailidis, D. A. Abanin, M. Serbyn, 36
14 and Z. Papić, *Phys. Rev. B* **98**, 155134 (2018). 37
- 15 [7] S. Bravyi, D. P. DiVincenzo, and D. Loss, *Ann. Phys.* 38
16 **326**, 2793 (2011). 39
- 17 [8] G. Vidal, *Phys. Rev. Lett.* **91**, 147902 (2003). 40
- 18 [9] J. Hauschild and F. Pollmann, *SciPost Phys. Lect. Notes* 41
19 **5** (2018), code available from [https://github.com/](https://github.com/tenpy/tenpy) 42
20 [tenpy/tenpy](https://github.com/tenpy/tenpy), [arXiv:1805.00055](https://arxiv.org/abs/1805.00055). 43
- 21 [10] J. C. Halimeh, R. Ott, I. P. McCulloch, B. Yang, and 44
22 P. Hauke, *Phys. Rev. Research* **2**, 033361 (2020). 45
- 23 [11] F. M. Surace, P. P. Mazza, G. Giudici, A. Lerose, 46
24 A. Gambassi, and M. Dalmonte, *Phys. Rev. X* **10**, 47
021041 (2020).
- [12] D. Bluvstein, A. Omran, H. Levine, A. Keesling, G. Semeghini, S. Ebadi, T. T. Wang, A. A. Michailidis, N. Maskara, W. W. Ho, S. Choi, M. Serbyn, M. Greiner, V. Vuletić, and M. D. Lukin, *Science* **371**, 1355 (2021).
- [13] N. Maskara, A. A. Michailidis, W. W. Ho, D. Bluvstein, S. Choi, M. D. Lukin, and M. Serbyn, *Phys. Rev. Lett.* **127**, 090602 (2021).
- [14] H. Bernien, S. Schwartz, A. Keesling, H. Levine, A. Omran, H. Pichler, S. Choi, A. S. Zibrov, M. Endres, M. Greiner, V. Vuletić, and M. D. Lukin, *Nature* **551**, 579 (2017).
- [15] B. Mukherjee, A. Sen, D. Sen, and K. Sengupta, *Phys. Rev. B* **102**, 075123 (2020).
- [16] J. M. Deutsch, *Phys. Rev. A* **43**, 2046 (1991).
- [17] M. Srednicki, *Phys. Rev. E* **50**, 888 (1994).
- [18] Z. Yao, L. Pan, S. Liu, and H. Zhai, “Quantum many-body scars and quantum criticality,” (2021), [arXiv:2108.05113](https://arxiv.org/abs/2108.05113) [[cond-mat.quant-gas](https://arxiv.org/abs/2108.05113)].
- [19] V. Oganesyan and D. A. Huse, *Phys. Rev. B* **75**, 155111 (2007).
- [20] V. Khemani, C. R. Laumann, and A. Chandran, *Phys. Rev. B* **99**, 161101 (2019).